Atmos. Chem. Phys. Discuss., 13, 30233–30285, 2013
www.atmos-chem-phys-discuss.net/13/30233/2013/
doi:10.5194/acpd-13-30233-2013

Atmospheric Chemistry and Physics Discussions

Temporal and spatial characteristics of ozone depletion events from measurements in the Arctic

J. W. Halfacre[1], T. N. Knepp[1,*], P. B. Shepson[1,2], C. R. Stephens[1,], K. A. Pratt[1,***], B. Li[3,****], P. K. Peterson[4], S. J. Walsh[4], W. R. Simpson[4], P. A. Matrai[5], J. W. Bottenheim[6], S. Netcheva[7], D. K. Perovich[8], and A. Richter[9]**

[1]Department of Chemistry, Purdue University, West Lafayette, Indiana, USA
[2]Department of Earth, Atmospheric, and Planetary Sciences, Purdue University, West Lafayette, Indiana, USA
[3]Department of Statistics, Purdue University, West Lafayette, Indiana, USA
[4]Department of Chemistry, University of Alaska, Fairbanks, Alaska, USA
[5]Bigelow Laboratory for Ocean Sciences, East Boothbay, Maine, USA
[6]Air Quality Research Division, Environment Canada, Toronto, Ontario, Canada
[7]Air Quality Processes Research Section, Environment Canada, Toronto, Ontario, Canada
[8]US Army Cold Regions Research and Engineering Laboratory, Fairbanks, Alaska, USA
[9]Institute of Environmental Physics, University of Bremen, Bremen, Germany
[*]now at: Science Systems and Applications, Inc., Hampton, Virginia, USA

**now at: Institute of Arctic and Alpine Research, University of Colorado at Boulder, Boulder, Colorado, USA
***now at: Department of Chemistry, University of Michigan, Ann Arbor, Michigan, USA
****now at: Department of Statistics, University Illinois at Urbana-Champaign, Urbana, Illinois, USA

Received: 9 October 2013 – Accepted: 4 November 2013 – Published: 19 November 2013

Correspondence to: J. W. Halfacre (jhalfacr@purdue.edu)

Published by Copernicus Publications on behalf of the European Geosciences Union.

ACPD
13, 30233–30285, 2013

Abstract

Following polar sunrise in the Arctic springtime, tropospheric ozone episodically decreases rapidly to near zero levels during ozone depletion events (ODEs). Many uncertainties remain in our understanding of ODE characteristics, including the temporal and spatial scales, as well as environmental drivers. Measurements of ozone, bromine monoxide (BrO), and meteorology were obtained during several deployments of autonomous, ice-tethered buoys (O-Buoys) from both coastal sites and over the Arctic Ocean; these data were used to characterize observed ODEs. Detected decreases in surface ozone levels during the onset of ODEs corresponded to a median estimated apparent ozone depletion timescale (based on chemistry and the advection of O_3-depleted air) of 11 h. If assumed to be dominated by chemistry, these timescales would correspond to larger-than-observed BrO mole fractions based on known chemical mechanisms and assumed other radical levels. Using backward air mass trajectories, the spatial scales for ODEs (defined by time periods in which ozone mole fraction $\leq 15\,\mathrm{nmol\,mol^{-1}}$) were estimated to be ~ 900 km (median), while areas estimated to represent major ozone depletions ($< 10\,\mathrm{nmol\,mol^{-1}}$) had dimensions of ~ 280 km (median). These observations point to a heterogeneous boundary layer with localized regions of active, ozone-destroying halogen chemistry, interspersed among larger regions of previously depleted air that retain reduced ozone levels through hindered atmospheric mixing. Based on the estimated size distribution, Monte Carlo simulations showed it was statistically possible that all ODEs observed could have originated upwind, followed by transport to the measurement site. Local wind speed averages were low during most ODEs (median of $\sim 3.6\,\mathrm{m\,s^{-1}}$), and there was no apparent dependence on local temperature.

ACPD
13, 30233–30285, 2013

1 Introduction

Global tropospheric oxidation is generally controlled by ozone (O_3), a major greenhouse gas (Gauss et al., 2006) and the most important precursor to the primary atmospheric oxidant, hydroxyl radical (OH) (Seinfeld and Pandis, 2006; Thompson, 1992). When the sun rises in the Arctic springtime (typically around mid-March), boundary layer O_3 often drops precipitously from background mole fractions of $\sim 40\,\mathrm{nmol\,mol^{-1}}$ (ppbv) to near zero levels for periods of hours, or even days, before recovering (Anlauf et al., 1994; Barrie et al., 1988; Bottenheim et al., 1986, 2002). During these ozone depletion events (ODEs), the prominent regional tropospheric oxidation pathways at the surface are driven by species other than OH radicals, notably Cl and Br atoms (Jobson et al., 1994).

ODEs are considered to start by the reaction of O_3 with photolytically active halogens, particularly bromine (R1) and (R2) (Simpson et al., 2007b).

$$Br_2 + h\nu \longrightarrow 2Br \quad \text{(R1)}$$

$$Br + O_3 \longrightarrow BrO + O_2 \quad \text{(R2)}$$

Atmospheric O_3 is removed in Reaction (R2) by Br to produce bromine monoxide (BrO). However, BrO is photolabile and can reproduce O_3 and Br in a null cycle. Therefore, the rate at which O_3 is destroyed is ultimately limited by the rate at which BrO reacts with another species to not reform O_3, such as in Reactions (R3–R5).

$$BrO + BrO \longrightarrow 2Br + O_2 \quad \text{(R3)}$$

$$BrO + ClO \longrightarrow OClO + Br \quad \text{(R4)}$$

$$BrO + HO_2 \longrightarrow HOBr + O_2 \quad \text{(R5)}$$

Ozone destruction is propagated by the regeneration of reactive halogen species. In the gas phase, Reactions (R3) and (R4) are believed to dominate at high halogen oxide concentrations, while (R5) is believed to play a larger role at smaller BrO levels (Le Bras and Platt, 1995; Piot and von Glasow, 2008). Reactions (R3) and (R4) directly reproduce reactive Br atoms, while the HOBr formed by Reaction (R5) must first undergo

ACPD
13, 30233–30285, 2013

photolysis (Simpson et al., 2007b, and references therein). Additionally, Reaction (R5) is also involved in a series of heterogeneous, autocatalytic reactions referred to as the "bromine explosion", which are believed to supply net atmospheric reactive bromine (Fan and Jacob, 1992; Tang and McConnell, 1996; Vogt et al., 1996; Wennberg, 1999). The "bromine explosion" involves the production of HOBr as above (R5), or through halogen reactions with oxidized nitrogen species (e.g. Aguzzi and Rossi, 2002; Hanson and Ravishankara, 1995). Uptake of this HOBr onto acidic, bromide-containing frozen surfaces produces Br_2 (Adams et al., 2002; Huff and Abbatt, 2002), which can then undergo the O_3 destroying reactions once photolyzed (R1). This series of reactions will exponentially increase Br_2 levels until some required reagent runs out.

Hypothesized sources of reactive halogens include saline frozen surfaces found across the Arctic Ocean, such as the snowpack, blowing snow, and sea salt-derived aerosols (Abbatt et al., 2012; Fan and Jacob, 1992; Frieß et al., 2011; Jones et al., 2009; Simpson et al., 2005; Yang et al., 2008). Recent in situ experiments showed that surface snowpacks (above sea ice or tundra) can act as efficient sources of Br_2, and that the "bromine explosion" can occur within the interstitial air of the snowpack, followed by release of the reactive bromine into the boundary layer via wind pumping and diffusion (Pratt et al., 2013).

Despite our increasing understanding of the role of halogens in ODEs, basic ODE characteristics, such as their temporal and spatial scales, remain unclear (Jacobi et al., 2010; Simpson et al., 2007b; Zeng et al., 2003). Current knowledge of O_3 depletion chemistry and the corresponding kinetics estimate the timescale for O_3 destruction to be on the order of days (Hausmann and Platt, 1994; Jobson et al., 1994; Piot and von Glasow, 2008, 2009; Tuckermann et al., 1997). However, there are only a few reports of Arctic ODEs that are assumed/known to have occurred primarily as a result of local scale chemistry (Boudries and Bottenheim, 2000; Jacobi et al., 2006). Given that the Arctic Ocean surface is sunlit, stable against vertical mixing, and ice-covered during the spring (Lehrer et al., 2004), it has been hypothesized that O_3-depleted surface air could be the norm in the Arctic boundary layer during this time and that O_3 is only ob-

ACPD
13, 30233–30285, 2013

served at the surface due to turbulent vertical mixing in an otherwise stable boundary layer. This vertical mixing can temporarily transport free tropospheric O_3 from aloft to the surface, raising the surface level mole fractions to between 30 and 40 nmol mol^{-1} (Bottenheim et al., 2009; Hopper et al., 1998; Jacobi et al., 2010; Strong et al., 2002; Zeng et al., 2003). Regarding the spatial scales of individual O_3-depleted air masses, Ridley et al. (2003) reported Arctic ODEs extending between 600 and 900 km in length from flights during the Tropospheric Ozone Production about the Spring Equinox experiment. Recently, Jones et al. (2013) reported the observation of multiple ODEs from a network of ten O_3 monitors spread over the Droning Maud Land sector of Antarctica, some of which scaled at least 1200 km in horizontal dimension. However, no such network of O_3 monitors has yet been established for the Arctic to make analogous observations.

In a study of long-term Arctic coastal measurements, Tarasick and Bottenheim (2002) observed that ODEs most often occurred at temperatures of less than 253 K, leading to the proposal that such low temperatures could be necessary for the initiation of ozone depletion. This hypothesis was strengthened by Adams et al. (2002), who reported that frozen NaCl/NaBr surfaces efficiently uptake and react with HOBr to both form and release gas phase Br_2 at temperatures below 253 K. This observation has been hypothesized to occur due to the precipitation of $NaCl \cdot 2H_2O$ at such temperatures, which then requires a greater concentration of Br^- to maintain the surface brine layer (Cho et al., 2002); when Cl^- precipitates, the volume of the brine water must decrease to maintain the ionic concentration needed for the appropriate freezing point depression. Boundary layer BrO enhancements have been correlated with low temperatures (Nghiem et al., 2012; Zeng et al., 2003), and seemingly linear increases in maximum BrO concentrations have been observed with decreasing temperatures, below 258 K (Pöhler et al., 2010). Additionally, strong positive correlations between O_3 concentration and potential temperature have been reported (Seabrook et al., 2011; Strong et al., 2002). However, Bottenheim et al. (2009) and Neuman et al. (2010) ob-

ACPD
13, 30233–30285, 2013

served ODEs at temperatures as high as 267 K, emphasizing uncertainty in the temperatures required for the observation of an O_3-depleted air mass.

ODEs have often been associated with a calm, stable boundary layer. Those observed under high wind speeds (faster than $10\,m\,s^{-1}$) are generally attributed to air mass transport (Simpson et al., 2007b). Yang et al. (2008) hypothesized that saline snow atop sea ice could disperse during periods of high wind and become a source of both sea-salt aerosol and bromine, consequently initiating ODEs. Indeed, there have been coastal-based studies in which increased BrO and aerosol were observed during periods of elevated wind speeds ($>5\,m\,s^{-1}$), and O_3 depletion sometimes, but not always, followed (Frieß et al., 2011; Jones et al., 2009). Higher wind speeds could also lead to better ventilation of the snowpack in which Br_2 is produced (Albert et al., 2002; Foster et al., 2001; Michalowski et al., 2000; Pratt et al., 2013; Toyota et al., 2011). Michalowski et al. (2000) discussed that the rate at which HOBr reacts with Br^- during Br_2 production in the "bromine explosion" was dependent on the time scale for turbulent diffusive transport of HOBr to the snowpack surface, which would be wind-speed dependent. However, due to few coincident observations of wind speeds, aerosol, O_3, and BrO, the dependence of ODEs on wind speed remains unclear.

Arctic air masses depleted in O_3 typically spend a significant amount of time over the Arctic Ocean before arriving at coastal measurement sites, suggesting that the ice-covered ocean is the most probable site of ODE initiation (Bottenheim and Chan, 2006; Gilman et al., 2010; Jacobi et al., 2006; Simpson et al., 2007a). In-situ chemical and meteorological data from the Arctic Ocean are, however, sparse. Most long-term Arctic tropospheric O_3 measurements have been made at coastal sites, and thus most observed ODEs have been attributed to the advection of an O_3-depleted air mass rather than local O_3 depletion chemistry (Morin et al., 2005; Simpson et al., 2007b). In attempts to examine ODE characteristics over the Arctic Ocean, studies have been conducted on ice floes (e.g., Hopper et al., 1994, 1998), aircraft (e.g., Jaeschke et al., 1999; Leaitch et al., 1994; Neuman et al., 2010; Ridley et al., 2003; Seabrook et al., 2013; Sheridan et al., 1993), and ships (e.g., Bottenheim et al., 2009; Gilman et al.,

ACPD
13, 30233–30285, 2013

2010; Jacobi et al., 2006; Pöhler et al., 2010; Seabrook et al., 2011). However, few of these studies have produced the long-term data required for in-depth studies of the temporal and spatial scales of ODEs.

Recently, a series of ice-tethered buoys were deployed as part of the Arctic Observing Network program to observe ODEs over the Arctic Ocean (Knepp et al., 2010). The buoys have been installed in sea ice for automated, continuous, long-term surface measurements of O_3, BrO (Carlson et al., 2010), carbon dioxide, and local meteorological conditions. The data generated by the O-Buoys represent the first long-term measurements of these chemical species directly over the surface of the ice-covered Arctic Ocean. Using this unique dataset, we estimate the timescales of O_3 depletion, examine the state of our understanding of the chemistry involved, and estimate the spatial extents and meteorological conditions supporting O_3-depleted air masses.

2 Experimental

2.1 Instrumentation

Surface O_3 and meteorology measurements discussed herein were collected during five separate deployments of O-Buoys (Table 1). Buoy deployment locations are shown in Fig. 1. Details of the O-Buoy design and operation are discussed extensively by Knepp et al. (2010), but a brief description of the meteorological, O_3, and BrO instruments are given herein. At the time of data analysis, BrO data were available from both O-Buoy1 during its Barrow, AK, deployment, and O-Buoy2 from the Beaufort Sea to compare with O_3 depletion timescales. The O-Buoy2 time series, including O_3, BrO, and temperature, is presented in Fig. 2. During winter months, O-Buoys are set to operate on an abbreviated sampling schedule to conserve power, typically sampling for a total of 4 h once every 1–3 days. The O-Buoys were switched to 24 h sampling every day close to the time of polar sunrise, typically near the end of February or early March.

ACPD
13, 30233–30285, 2013

The MAX-DOAS instrument was an exception to this sampling schedule as it was kept unpowered during the winter months, and turned on during the switch to 24 h sampling.

Temperature was measured using a Vaisala model HMP45C temperature and relative humidity probe. Wind speed was measured using a RM Young Model 05103 anemometer. The range of wind speeds observed across the four O-Buoys deployed was 0–15 m s^{-1}. It was observed in the 2009 Barrow, AK, O-Buoy1 deployment, however, that the anemometer was susceptible to icing, which would impede its ability to spin freely and provide accurate measurements. This effect was most prominent during the 2009 Barrow, AK, deployment of O-Buoy1, in which wind speed fell from a mean of about 2 m s^{-1} to 0 m s^{-1} for a period of four days. To mitigate the impact of this effect on the interpretation of the results, wind data were not utilized in our analysis when wind speed was measured as 0 m s^{-1}. While there is reason to believe that wind speeds are indeed low during these periods, the actual wind speed is unknown. Thus, if the average wind speed calculated during an ODE contained > 50 % of such values, the wind data for that event were not included in the data analysis. We also acknowledge that an icing effect could create a measurement bias toward lower values. However, as discussed in the text (Sect. 3.3), on average this appears to be a minor issue in terms of our use of the anemometer data (e.g. to calculate ODE spatial scales) as we find effectively equivalent results using our anemometer wind speeds and those estimated using the HYSPLIT backwards trajectory model (Sect. 2.3).

Ozone was measured using custom-built 2B Technologies model 205 dual-beam O_3 monitors. Customizations include one backup pump, one backup O_3 scrubber, a lamp heater, and modified firmware to control the instrument remotely. The instrument inlet, which contained a 90 mm quartz fiber filter (Pall Life Sciences) to prevent intake of large particles, is located on the mast of the buoy ∼ 2 m above the sea ice, while the instrument itself is located inside the hull of the buoy beneath the sea ice such that it operates under a near constant temperature (∼ −1.5 °C). The O_3 instrument did not display a temperature-dependence during laboratory, pre-deployment O_3 calibrations as long as the cell temperature of the instrument was stable; cell temperature

ACPD
13, 30233–30285, 2013

stabilization generally occurred after 20–30 min, and the first 30 min of O_3 data during these warm-up periods were excluded from data analysis. The instrument has a manufacturer specified limit of detection of 1 nmol mol^{-1}, and individual measurement uncertainty was calculated to range from 2.1–3.5 nmol mol^{-1}. Sample averaging by the ozone monitors differed between buoy deployments: O-Buoy1 used 10 s averages, O-Buoy3 used two second averages, and both O-Buoy2 and O-Buoy 4 used one minute averages. For analysis, all data were smoothed to 5 min moving averages.

BrO was detected using a multi-axis differential optical absorption spectroscopy (MAX-DOAS) instrument. The scan head telescope, located at the top of the buoy mast, collects scattered radiation and sends it through a fiber optic cable to the computer/spectrometer module, which consists of a single board computer (Technologic Systems TS-7260), a stepper motor driver (Stepperboard BC2D15), interface electronics, and a miniature spectrometer (Ocean Optics HR2000, 318–455 nm). The scan elevation angle is controlled by the O-Buoy's supervisory computer and observes light at angles of 90 (zenith), 20, 10, 5, 2, and 1 ° over a period of 30 min (Carlson et al., 2010). The zenith spectrum from a 30 min data measurement period was used as the reference spectrum for the lower elevation angle spectra, which minimizes the differential absorption by stratospheric species. To obtain differential slant column densities (dSCD), the QDOAS software was used (Fayt et al., 2011) to fit both the logarithm of the ratio of each low elevation spectra and zenith spectra in the wavelength region 346–364 nm (convolved absorber cross sections detailed in Table 2), as well as a 3rd order polynomial to account for broadband features and a spectral offset to account for stray light. Fit residuals for both O-Buoy1 and O-Buoy2 were less than 1×10^{-3} resulting in BrO dSCD errors less than 4×10^{13} molecules cm^{-2} and O_4 dSCD errors of less than 1×10^{42} molecules^2 cm^{-5}. Retrieval of BrO mole fractions from dSCD data is a two-step inverse problem. First, the aerosol profile is determined from O_4 dSCDs using both the SCIATRAN radiative transfer model as a forward model, and the estimation techniques detailed in Frieß et al. (2006). Then, a vertical profile of BrO mole fractions from the ground to 2 km (100 m intervals) was obtained using both the radiative transfer model

ACPD
13, 30233–30285, 2013

McArtim (Deutschmann et al., 2011) as a forward model, and similar optimal estimation techniques detailed in Frieß et al. (2011). Because we are only considering surface O_3 measurements, only the average BrO mole fractions in the lowest 100 m were used in subsequent portions of the study.

The BrO detection limit is a function of the geometry of the observation and the state of the atmosphere at the time of the measurement. The detection limits for the BrO dSCDs varied between 2 and 4×10^{13} molcm^{-2} in each deployment. To evaluate the error associated with the retrieved surface mole fractions, it is necessary to consider both dSCD measurement error and smoothing error (Rodgers, 2000). Smoothing error calculations quantify the error resulting from the inability of the instrument to observe fine structure in the vertical profile. The smoothing error was estimated through considering the mean of an ensemble of profiles retrieved in late summer ($\bar{x}$) when the dSCD measurements indicated no measurable BrO. This allowed us to assume the actual profile (x_a) is given by 0 pmol mol^{-1} (pptv) BrO through 2 km. The average surface mole fraction smoothing errors (ϵ_s) for the entire O-Buoy2 campaign were estimated using Eq. (1), where **A** represents the averaging kernel matrix and **I** is the identity matrix (Rodgers, 2000).

$$\epsilon_s = (\mathbf{A} - \mathbf{I})(\bar{x} - x_a) \quad (1)$$

Individual surface mole fraction errors due to smoothing error averaged 0.3 pmol mol^{-1} for the O-Buoy2 campaign. Including individual mole fraction errors due to propagated dSCD measurement error, total surface mole fraction errors range from 0.7 to 6.9 pmol mol^{-1}, with average and median errors corresponding to $\sim$ 3.0 and 3.3 pmol mol^{-1} respectively. Due to the timing of the O-Buoy1 deployment, we were unable to estimate smoothing error in the manner described above. Therefore, only errors due to propagated dSCD measurement error were considered. For O-Buoy1, total surface mole fraction errors range from 0.7 to 4.5 pmol mol^{-1}, with average and median errors corresponding to $\sim$ 2.5 and 2.6 pmol mol^{-1} respectively.

ACPD
13, 30233–30285, 2013

2.2 ODE definition

Several definitions of ODE conditions can be found throughout the literature. For example, some studies define an ODE, partial or severe, as when O_3 mixing ratios are below 20 nmol mol^{-1} (Ridley et al., 2003), 10 nmol mol^{-1} (Tarasick and Bottenheim, 2002), 5 nmol mol^{-1} (Bottenheim et al., 2009; Frieß et al., 2011; Jacobi et al., 2010), or 4 nmol mol^{-1} (Piot and von Glasow, 2008, 2009; Ridley et al., 2003). For this study, a specific set of ODE criteria, defined below, were developed to examine ODEs identified using the O-Buoy data set. We define and distinguish periods of "major" ozone depletion events (MODEs; defined differently here than originally defined by Ridley et al., 2003, see below) from a less severe ODE term to enable us to compare and contrast the temporal and spatial differences between them. Note that as defined below, any ODE can include the shorter periods of MODEs, but the MODE criteria are not necessary for an event to be defined as an ODE. These criteria are visually illustrated in Fig. 3 using sample O-Buoy data.

Background O_3 conditions were considered to be established if O_3 mole fractions stayed above 25 nmol mol^{-1} for longer than 12 h. If O_3 dropped below 15 nmol mol^{-1} for longer than one hour, the event was considered to be an ODE, with the ODE start time defined as the time at which O_3 drops below 90 % of its local maximum concentration prior to depletion. If O_3 subsequently rose above 25 nmol mol^{-1} for longer than 12 h, the ODE was considered terminated; the ODE end time was defined as the time when O_3 reached 90 % of the local maximum O_3 mole fraction after rising above 25 nmol mol^{-1} for more than 12 h. It should be noted that the increase in O_3 mole fraction on 17 April 2011 seen in Fig. 3 does not recover above 25 nmol mol^{-1} for longer than 12 h, and its subsequent decrease does not represent a new ODE. For the calculation of the O_3 depletion timescale, an O_3 decrease stop time was defined as the time at which O_3 first reached 10 % of the difference of the preceding maximum and ultimate minimum O_3 mole fractions during the ODE.

ACPD
13, 30233–30285, 2013

MODEs are cases for which O_3 dropped below 10 nmol mol^{-1} for longer than one hour, with the start time defined as the time at which O_3 fell below 10 nmol mol^{-1}. If O_3 then increased above 10 nmol mol^{-1} for longer than 12 h, the MODE is considered terminated, with the MODE stop time defined as the time at which O_3 recovered above 10 nmol mol^{-1}.

2.3 Air mass trajectory analysis

The NOAA HYSPLIT air mass trajectory model (Draxler and Hess, 1997, 1998; Draxler, 1999) was utilized to examine air mass trajectories corresponding to O_3-depleted air masses, as defined in Sect. 2.2. Backward air mass trajectories were calculated starting from a height of 10 m a.g.l. using the ODE stop time as the start time of the model for the backward trajectory. Isobaric trajectories were chosen because the stable surface air in which the ODEs occur is typically well isolated from the air aloft (Oltmans et al., 2012; Seabrook et al., 2013); as long as O_3 is in ODE conditions, the air is likely to be surface layer air. The trajectory lengths utilized were defined by the ODE durations (see Fig. S1 for the distribution of ODE time lengths), such that the "endpoints" of the backward trajectories corresponded to the defined ODE start times. ODE spatial scales were defined as the maximum distance between any two points of the backward air mass trajectory (illustrated visually in Fig. 4). This analysis was performed for both the broader ODE definition and MODEs.

The HYSPLIT model was also used to estimate some meteorological parameters at each position along the backward trajectory. For this analysis, the average air temperature along each trajectory was compared with the temperatures recorded by the O-Buoy. The path lengths and time lengths of individual trajectories were used to estimate the average wind speeds of the air masses, which were compared with the wind speeds obtained from the O-Buoy anemometer. Wind rose plots were created based on the quadrant in which the air mass trajectory spent the most time during a given ODE (north (315–45°), south (135–225°), east (45–135°), and west (225–315°)). Only

ACPD
13, 30233–30285, 2013

four quadrants were used in the wind rose plots because there is a large level of uncertainty associated with using a back trajectory model for this purpose (Kahl, 1993). These angles were obtained by calculating the bearing between the O-Buoy and each point along each back trajectory for each ODE.

2.4 Monte Carlo experiment

A Monte Carlo experiment was performed to provide statistical support to the hypothesis that the observed ODEs represent depletion that is initiated upwind, and that the depleted air mass then travels to the point of observation. For this simulation experiment, we estimated the probability that assumed circular depletion regions overlap with a point of interest (an O-Buoy) when randomly placed about a defined area (the ice-covered Arctic Ocean). The diameters of the circles were defined by the ODE size distribution derived from O-Buoy1 and O-Buoy2 Beaufort Sea observations (Sect. 2.3); these particular ODEs were chosen for this exercise because of the similar locations and drift trajectories of the buoys, providing the needed statistics for the analysis. Eighteen ODEs were observed between the two deployments (in 2010 and 2011), with ODE sizes ranging from 210–3532 km (Fig. S2). The circles, with sizes taken from the observed size distribution, were simultaneously and randomly placed in an area defined by the average sea ice extent of the Arctic Ocean between March 2010 and 2011 (Fig. 5), as reported by the National Snow & Ice Data Center (http://www.nsidc.org/). We note, however, that the largest ODE size, observed by O-Buoy2 (diameter of 3532 km), was estimated to be larger than the defined sea ice extent and was excluded from the simulations. Thus, a total of seventeen circles were used in these simulations. The number of circles that overlapped with the location of the buoy (assumed to be 74.75° N, 142° W, an approximate location of both O-Buoys 1 and 2) was determined for multiple iterations of the placement of the 17 circles. Figure 5 represents one iteration of the experiment, which was repeated 2000 times in order to obtain a statistical distribution of the number of overlaps. Additionally, a sequence of similar Monte Carlo experiments was repeated for individual ODE sizes 1000 times to obtain the probability

ACPD
13, 30233–30285, 2013

that each circle size overlaps with the location of the buoy. This simulation experiment was conducted to examine the relationship between ODE size and the probability that the ODE would only be observed as a transport event.

3 Results and discussion

3.1 Ozone depletion timescale

For O-Buoys 1–4, a total of 38 ODEs were observed between February and June. On the assumption that O_3 decrease is an exponential decay process, and to express the observed depletion time scales in an objective manner, the apparent O_3 depletion timescale (τ_{O_3}) at the beginning of an ODE was estimated as the reciprocal of the slope of $\ln[O_3]$ vs. time (during the period ODE start time–O_3 decrease stop time, as discussed in Sect. 2.2). This time scale is observed due to a combination of both halogen chemistry and the advection of O_3-depleted air past the buoy, though the extent to which each factor affects τ_{O_3} is unknown. As seen in Fig. 6a, τ_{O_3} ranged from 30 min to 14 days, with the majority (76 %) shorter than 24 h (median τ_{O_3} of 11 h). These timescales correspond to O_3 decrease rates ($-\frac{d[O_3]}{dt}$) that range between 0.02 and 30 nmol mol^{-1} h^{-1} (average and standard deviation: 3.5 ± 5.4 nmol mol^{-1} h^{-1}). By comparison, Tuckermann et al. (1997) reported O_3 decrease rates ranging from 0.24 and 7 nmol mol^{-1} h^{-1} from their measurements in Ny-Ålesund, Spitsbergen. Removing coastal site data (O-Buoy1 2009, deployed in Barrow, AK) from the histogram did not significantly alter the τ_{O_3} distribution. For the six ODEs with τ_{O_3} equal to 50 h or longer, two cases occurred in June after changes in O_3 levels had become much more gradual, relative to the sporadic and episodic nature of the preceding months (February through May). Apart from these two events, which occurred at higher temperatures, there was no clear difference in the local average wind speeds or temperatures that was unique to the remaining four of these six events.

ACPD
13, 30233–30285, 2013

If the observed ODEs were indeed driven by local chemistry occurring at the location of the O-Buoys (i.e. the effect of advection is minimized in the apparent τ_{O_3}), it is surprising that the majority of cases featured such short apparent timescales of O_3-depletion ($\tau_{O_3} < 12$ h). Most previous model estimates of O_3-depletion timescales due to chemistry are on the order of days (Hausmann and Platt, 1994; Jobson et al., 1994; Piot and von Glasow, 2008, 2009; Tuckermann et al., 1997). Generally, periods of fast O_3 depletion observed at coastal sites have been attributed to the transport of O_3-depleted air masses over the measurement site. In these cases, O_3 has been hypothesized to be chemically destroyed upwind (i.e. over the Arctic Ocean), and the apparent τ_{O_3} is a function of both the rate at which the O_3-depleted air mass travels across the measurement site, and the horizontal concentration gradient at the edges of those air masses. For example, Morin et al. (2005) observed O_3 levels to fall from mole fractions of $\sim 30\,\mathrm{nmol\,mol^{-1}}$ to less than $5\,\mathrm{nmol\,mol^{-1}}$ in around 3 min from over the Arctic Ocean, 6 km off the coast of Alert, Canada. However, fast O_3 depletion attributed to local chemistry has been previously reported: using measurements from aboard the icebreaker RV *Polarstern* in the Arctic Ocean, Jacobi et al. (2006) observed a decrease in O_3 from $40\,\mathrm{nmol\,mol^{-1}}$ to $< 1\,\mathrm{nmol\,mol^{-1}}$ in less than 7 h.

To interpret the results from the O-Buoys, we first explore the extent to which known chemical mechanisms could account for the fast rates of O_3 decrease. Rates of O_3 loss during ODEs have been previously thought to be limited by Reactions (R3)–(R4) at high BrO levels, estimated by Eq. (2) below (Le Bras and Platt, 1995; Platt and Janssen, 1995).

$$\left(-\frac{\mathrm{d}[O_3]}{\mathrm{d}t}\right) = 2k_{\mathrm{BrO+BrO}}[\mathrm{BrO}]^2 + 2k_{\mathrm{BrO+ClO}}[\mathrm{BrO}][\mathrm{ClO}] \quad (2)$$

Recently, Stephens et al. (2013b), using a 0-D model constrained by chemical data collected during the 2009 OASIS field campaign, found that Br-atom destruction of O_3 has a low homogeneous gas phase radical propagation chain length (close to 1). Because of this small chain length, the dominant source of Br atoms that destroy O_3 appears to

ACPD
13, 30233–30285, 2013

be from the photolysis of Br_2 and BrCl emitted from the surface or aerosols (Stephens et al., 2013b), and thus most of the BrO that is produced terminates via reaction with HO_2 (R5) (or NO_2 for more polluted areas, such as Barrow, AK). This pathway would result in more heterogeneous recycling of Br atoms. They then compared $\frac{d[O_3]}{dt}$ as calculated by both Eq. (2) and by the net chemical O_3-destruction rate (Eq. 3).

$$\left(-\frac{d[O_3]}{dt}\right) = k[Br][O_3] + k[Cl][O_3] + k\left[O(^1D)\right][H_2O] + k[OH][O_3] + k\left[HO_2\right][O_3] - k[BrO][NO] - J[BrO] - k[ClO][NO] - J[ClO] \quad (3)$$

In calculating $\frac{d[O_3]}{dt}$, a regression between the rates showed that using only Eq. (2) underestimates $\frac{d[O_3]}{dt}$ (from Eq. 3) by a factor of 3.6 on average (Stephens et al., 2013b). Therefore, we estimate the BrO mole fractions required to cause the observed rates of O_3 depletion according to Eqs. (4) and (5) below (Stephens et al., 2013b). These equations include the factor of 3.6 that accounts for the production of bromine atoms via Br_2 and BrCl photolysis, two molecular halogens derived from heterogeneous recycling of species such as HOBr and $BrONO_2$ on halide-containing aerosols or the saline snowpack (Abbatt et al., 2012; Simpson et al., 2007b). A constant ClO concentration of 1.7×10^8 molecules cm^{-3} (6 pmol mol^{-1} at 248 K and atmospheric pressure) was assumed based on average concentrations measured during the 2009 OASIS campaign (Stephens, 2012).

$$\left(-\frac{d[O_3]}{dt}\right) = 3.6 \times \left(2k_{BrO+BrO}[BrO]^2 + 2k_{BrO+ClO}[BrO][ClO]\right) \quad (4)$$

$$\tau_{O_3} = \frac{[O_3]_{avg}}{3.6 \times (2k[BrO]^2 + 2k[BrO][ClO])} \quad (5)$$

Because Stephens et al. (2013b) utilized a temperature of 248 K in their model, consistent with average local temperatures at Arctic coastal sites in the springtime,

ACPD
13, 30233–30285, 2013

we estimate BrO mole fractions at this temperature in order to utilize the factor of 3.6. The rate constants $k_{BrO+BrO} = 3.8 \times 10^{-12}$ cm^3 molecules^{-1} s^{-1} and $k_{BrO+ClO} = 8.7 \times 10^{-12}$ cm^3 molecules^{-1} s^{-1} were calculated based on Sander et al. (2011). The calculated BrO mole fractions corresponding to the estimated τ_{O_3} range from ~ 1 pmol mol^{-1} (τ_{O_3} = 356 h) to 122 pmol mol^{-1} (τ_{O_3} = 28 min), with a median of 17 pmol mol^{-1} (Fig. 6b). The majority of the calculated distribution of BrO required is fairly comparable to previously reported enhanced surface BrO mole fractions, which often peak around 20–40 pmol mol^{-1} (Hausmann and Platt, 1994; Hönninger et al., 2004b; Pöhler et al., 2010; Tuckermann et al., 1997). Indeed, 31 out of 38 events were calculated to require less than 40 pmol mol^{-1} of BrO for O_3 depletion. For the O-Buoy1 (Barrow, AK) and O-Buoy2 deployments, MAX-DOAS BrO data are available for comparison with the calculated BrO estimations (Fig. 6b and c; Table 3). Though the MAX-DOAS BrO mole fractions exhibit maxima higher than 20 pmol mol^{-1} throughout the spring (ex. Fig. 2), the average BrO mole fractions during periods of O_3 decrease (ODE start time – O_3 decrease stop time; Sect. 2.2) were found to be less than 20 pmol mol^{-1} (Table 3).

The amount of BrO data available was dependent on the length of daylight, as the MAX-DOAS is a passive instrument (Carlson et al., 2010). In the case of O-Buoy1 at Barrow, there were not enough BrO data available for most periods of O_3 decrease to produce solid conclusions. However, observed BrO levels for three events were not inconsistent with the calculated BrO levels required for the observed τ_{O_3} (see Table S1 and Fig. S3). While these three events do not have enough BrO data to merit an in-depth discussion, they are discussed in more detail in the Supplement. For the remaining cases in which there were enough BrO data to make comparisons, observed BrO levels were found to be lower than the calculated BrO required by Eqs. (4) and (5), as also found and discussed for the greater BrO data set for O-Buoy2.

The estimated BrO mole fractions required for each τ_{O_3} observed by O-Buoy2 in the Beaufort Sea is greater than the BrO actually observed during each period of O_3 de-

ACPD
13, 30233–30285, 2013

crease, even when considering the propagated measurement error (Table 3; described in Sect. 2.1). This result is surprising since the Arctic Ocean is the assumed originating site for ODEs. At least for O-Buoy2, the observed BrO, assumed 6 pmol mol^{-1} ClO, and factor of 3.6 from Stephens et al. (2013b) cannot account for the apparent τ_{O_3}.

Possible reasons for the observed small τ_{O_3} values can be summarized by the following two hypotheses:

(1) There are chemical mechanisms for O_3 destruction that are currently not being considered, or other radical levels (e.g. IO, ClO, HO_2) are higher than assumed here.

(2) Most ODEs occur upwind of the O-Buoys such that the observed O_3 depletion timescales largely represent air mass transport, as discussed above.

Concerning the first hypothesis, iodine radical chemistry has been observed in Antarctica (Saiz-Lopez et al., 2007) and in the sub-Arctic at Hudson Bay (Mahajan et al., 2010). Iodine chemistry has been shown by models to have a significant impact on O_3 destruction chemistry due to the very fast rate constant for IO reaction with BrO ($\sim$ 127 times faster than Reaction R3) (Calvert and Lindberg, 2004; Stephens et al., 2013a). Stephens et al. (2013a) show that even if only 0.8 pmol mol^{-1} of IO were present, the rate of conversion from BrO to Br would increase by $\sim$ 2, using $k_{(IO+BrO)} = 3.8 \times 10^{-10}$ cm^3 molecule^{-1} s^{-1} at 248 K, which would yield O_3 depletion timescales during ODEs similar to the ones observed by this study. Though previous studies have indicated the presence of active iodine chemistry through enhanced levels of total iodine (Martinez et al., 1999) and filterable iodine (Barrie et al., 1994; Schall and Heumann, 1993), there are no measurements of IO in the high Arctic above long path DOAS limits of detection as low as 0.3 pmol mol^{-1} (Pöhler et al., 2010), nor are there estimates of I_2 mole fractions for the Arctic Ocean region. Thus, this possible mechanism remains purely speculative. The salinity of first year ice could be a reason for enhanced chlorine radical production as compared to coastal (e.g. Barrow) observations, or snowpack sources of HO_x (HONO, Zhou et al., 2001, HCHO, Sumner and Shepson, 1999; Sumner et al., 2002, or H_2O_2, Hutterli et al., 2001; Jacobi et al., 2002) could enhance HO_2 levels and thus reactivity.

ACPD
13, 30233–30285, 2013

We can potentially test for missing chemistry by examining the distribution of the ozone tendency, ($\frac{d[O_3]}{dt}$), with and without the calculated component from known chemistry (as defined in Eq. 4). First, the observed short-term ozone tendency was calculated for values of dt between consecutive BrO measurements (currently O-Buoy1 at Barrow, and O-Buoy2 in the Beaufort Sea) and plotted in Fig. 7a and b. Both distributions are zero centered (average Barrow: 0.15 nmol mol^{-1} h^{-1}; average Beaufort: 0.01 nmol mol^{-1} h^{-1}) with heavy tails on each side. Then, $\frac{d[O_3]}{dt}$ was calculated using Eq. (4), as above (Fig. 7c and d); this represents the component of the observed $\frac{d[O_3]}{dt}$ resulting from O_3 depletion chemistry. By subtracting these two results, we obtain the distribution of ozone tendencies not accounted for by the considered chemical mechanisms (Fig. 7e and f). These two distributions (representing all observations, and those with known chemistry removed) do differ significantly after this subtraction at the 95 % confidence level according to the Kolmogorov–Smirnov test (p value = 4.9×10^{-4} and 1.4×10^{-6} for the O-Buoy1 and 2 results, respectively). Both distribution averages become more shifted from zero, with an average $\frac{d[O_3]}{dt}$ of −0.43 nmol mol^{-1} h^{-1} for O-Buoy1, and −0.18 nmol mol^{-1} h^{-1} for O-Buoy2. However, it can be shown that the overall symmetry does slightly improve after subtraction by calculating skewness (Eq. 6),

$$\text{skewness} = \frac{\sum_{i=1}^{N}(x_i - \bar{x})^3}{(N-1)s^3} \quad (6)$$

where N represents the number of measurements and s represents the standard deviation of a sample. Skewness increases from −0.38 to −0.25 for the O-Buoy1 at Barrow case, and from −0.82 to −0.80 in the O-Buoy2 in the Beaufort Sea case. Springtime chemical O_3 production in the Arctic boundary layer has been found to be essentially negligible (Helmig et al., 2009, 2012), and so it is likely the positive portions of these distributions result from air mass transport and vertical mixing. This analysis then produces a result not inconsistent with the idea that the remainder of the negative $\frac{d[O_3]}{dt}$ represents air mass transport.

ACPD
13, 30233–30285, 2013

Hypothesis two, involving atmospheric transport, is in line with those of many previous studies (e.g., Bottenheim et al., 2009; Hausmann and Platt, 1994; Jacobi et al., 2010; Morin et al., 2005). As discussed in these studies, fast O_3 depletion can often be attributed to changes in air mass flow, and surface O_3 mole fractions can return to background levels upon the passage of low-pressure systems, with associated enhanced vertical mixing. The idea that most of the negative side of the ozone tendency distribution results from transport and not local chemistry is statistically possible only if the average spatial scale of an ODE region is below some critical size (discussed below in Sect. 3.2).

3.2 ODE spatial scales

To estimate the spatial scales of ODEs, we combine O-Buoy observations with backward air mass trajectory analysis (Sect. 2.3), as shown in Fig. 8 for ODEs and MODEs. This analysis assumes O_3 depletes within an air mass upwind, and this O_3-depleted air mass subsequently roams across the measurement site, such that the size of the air mass can be estimated from the length of time O_3 is depleted and the wind speed. We note, however, that the observations likely involve some combination of both transport and local chemistry, given O-Buoy measurements of BrO. It is of course conceptually possible that other scenarios exist; for instance, conditions could exist in some region upwind that result in the continuous depletion of O_3-containing air masses that pass over this region. This depleted air may then pass over the buoy. If the depleted air remains intact, however, the spatial scale calculations would still apply.

As shown in Fig. 8, the mode of the one-dimensional length for the ODEs was ~ 908 km. While the estimated size distribution of the MODEs ($O_3 < 10$ nmol mol^{-1}) showed no clear mode, it is clear that the distribution contains mostly (relatively) smaller events, with a median size of 282 km. The distribution of results is also consistent with observations by Jones et al. (2013) and Ridley et al. (2003), who both reported ODEs of spatial dimensions of at least 1200 km and between 600 and 900 km, respectively. These results strongly suggest that large areas of the Arctic are at least partially de-

ACPD
13, 30233–30285, 2013

pleted during Arctic springtime with local embedded areas that are more depleted. While these isobaric trajectories likely represent the near-surface transport path of depleted air (Seabrook et al., 2013), we also estimated the ODE spatial scales using isentropic back trajectories and the local wind speeds using the O-Buoy anemometer. The means for the isobaric- (1160 ± 374 km), isentropic- (1260 ± 279 km), and local wind speed-based (1154 ± 341) spatial scale distributions were statistically similar at the 95 % confidence level (confidence intervals reported here).

As discussed in Sect. 3.1, known chemical mechanisms with reasonable levels of other radicals could not account for the observed time scales of O_3 depletion, which suggests the fast O_3 depletion timescales we observed were due in large part to the advection of previously depleted air. A Monte Carlo simulation experiment was conducted with the aim of examining the statistical probability that all observed ODEs, based on the general ODE definition ($O_3 \leq 15\,\mathrm{nmol\,mol^{-1}}$), could have occurred non-locally to the buoy. As described in Sect. 2.4, the simulations were conducted by randomly placing circles (hypothetical ODEs/source regions) across an area the size of the Arctic Ocean sea ice. These circles were defined using the distribution of ODE spatial scales determined from the 17 events observed by the O-Buoy1 and O-Buoy2 deployments (Fig. S2), which observed O_3-depleted air ∼ 60 % of the time between late March and May 2010 and ∼ 65 % of the time between mid April and May 2011, respectively. For this statistical exercise, we made the assumptions that the circles could appear (initiate) anywhere across the Arctic Ocean, and that the circles could also represent possible sizes of ODE source regions. While there is evidence to suggest the existence of specific source regions favorable to ODE formation (Bottenheim and Chan, 2006; Bottenheim et al., 2009; Koo et al., 2012; Simpson et al., 2007a; Theys et al., 2011), no definitive conclusions have yet been made from in-situ observations regarding the locations nor the sizes of such regions. We also assume that that the circle must be contained wholly within the bounds shown in Fig. 5 in order to equally represent all sizes from the distribution. We acknowledge that this assumption could overestimate the frequency with which ODEs overlap with the buoy, as ODEs

ACPD
13, 30233–30285, 2013

have been observed in sub-Arctic regions, such as Kangerlussuaq, Greenland (67° N, 51° W; Miller et al., 1997), and Hudson Bay (55° N, 75° W; Hönninger et al., 2004a). However, this approach could also underestimate the frequency of overlap, as ODEs that initiate remotely from the buoy would be less likely to be part of the observed distribution of events; in other words, it is also possible that the study region for the Monte Carlo simulation could be too large. It is also assumed that the circles represent fully formed O_3-depleted air masses or source regions, and that a circle overlapping with the buoy represents "local" ODE initiation relative to the O-Buoy.

The Monte Carlo simulations show that the randomly placed circles most often do not overlap with the measurement site (Fig. 9a). In fact, only very large sizes (larger than ~ 1750 km) were likely to intercept the O-buoy location with a significant probability (> 10 %), as shown in Fig. 9b. Specifically, none of the 17 circles overlapped with the O-Buoy site in 58 % of the 2000 simulation iterations, and only one circle (in 17) overlapped with the O-Buoy site in 33 % of iterations. Therefore, the spatial statistics support the possibility that the overwhelming majority of ODEs observed in this study could have initiated upwind of the O-Buoy locations in the Beaufort Sea. We emphasize that this Monte Carlo exercise does not prove that this is the case, only that this hypothesis is not inconsistent with the observed ODE spatial scales. The practical question is then raised as to how many buoys (observation sites) must be present to increase the probability of observing an ODE primarily due to local chemistry (with the assumption of equal probability of initiation across the Arctic Ocean and that ODE sizes represent source regions, as assumed for the Monte Carlo experiment). If, for example, two additional O-Buoys were deployed at the North Pole (86° N, 54° W) and in the East Siberian Sea (75° N, 170° E), both potential sites of future O-Buoy deployments, repeating the simulations showed that five out of 17 circles overlapped with at least one measurement site, with no simulation iterations resulting in zero circle overlaps (Fig. S4). This result emphasizes the need for multiple, simultaneous deployments of O-Buoys across different geographical regions to ensure that local scale chemistry is observed within one deployment season.

ACPD
13, 30233–30285, 2013

To examine if there is a consistent upwind region from which ODEs travel, wind rose plots were constructed for the ODEs observed by O-Buoy1 and O-Buoy2 in the Beaufort Sea, as shown in Fig. 10. As above, the O-Buoys deployed in the Beaufort Sea were chosen because of their similar locations and drift trajectories, providing the needed statistics for the analysis. During ODEs, air masses most commonly traveled from the east (~ 39 % of cases), followed by the north (~ 33 % of cases) and the west (~ 22 % of cases). For the MODE air masses, the trajectories again most often originated from the eastern sector (~ 41 % of cases; Fig. 10b), and the northern and western sectors accounted for ~ 27 % of cases each. Only one event showed an air mass originating from the south, toward the Alaskan and Canadian coasts. These results support a hypothesis that all regions that are sea-ice covered can support ODE chemistry. Notably, the region to the east of the buoys (i.e. from the Canadian archipelago and eastern Beaufort Sea) features sea ice that historically contains a high fraction of multi-year ice (Kwok et al., 2009), and GOME satellite imagery has previously shown large amounts of BrO to be present in this region (Choi et al., 2012; Koo et al., 2012; Richter et al., 1998; Salawitch et al., 2010). For the coastal sites of Alert, Canada, and Zeppelinfjellet, Svalbard, Bottenheim and Chan (2006) have previously used air mass trajectories to suggest that ODE air mass source regions were in the East Siberian Sea, an area to the northwest of the O-Buoys that features first year ice that breaks up in spring. It should be noted, however, that Bottenheim and Chan (2006) only reported trends during springtime for the month of April, as opposed to this study that examined ODEs from as early as February to as late as June (Table 1 and Fig. 2). Unfortunately, there were not enough events per month to observe any clear monthly source region trends. Additional simultaneous O-Buoy measurements are needed to compare the concentrations of ozone and halogens above likely source regions across the Arctic Ocean.

ACPD
13, 30233–30285, 2013

3.3 Temperature and wind speed during ODEs

Figure 11 shows the distribution of temperatures that applied during the ODEs. In this study, ODEs were observed at local temperatures between 243 K and 273 K (Fig. 11a), and ~ 66 % of the ODEs occurred at temperatures greater than 253 K. This result shows that lower temperatures were not necessary to observe ozone-depleted air masses, corroborating the conclusions of Bottenheim et al. (2009) and Jacobi et al. (2010). Indeed, the apparent mode of the distribution (261 K) is 8 K warmer than the hypothesized required upper limit temperature to result in rapid ozone depletion. The temperatures for MODEs resulted in a similar distribution (Fig. 11b). An illustrative event is shown in Fig. 2; the O-Buoy2 ODE occurring in early June shows a noticeable increase in BrO while temperatures average around 270 K. If however ODEs most often originate upwind from the site of O-Buoys, the temperatures at the observation site could be irrelevant, as the actual depletion chemistry may have taken place at a location where the temperature was much lower. To examine this, the HYSPLIT backward air mass trajectories were utilized to estimate the average temperatures experienced by the observed air mass upwind. In Fig. 11c and d, we present histograms of the average temperatures over each air mass trajectory for both ODEs and MODEs, which were observed to be very similar (medians: ~ 258 K and 257 K for ODE and MODE, respectively). These HYSPLIT-derived temperature distributions were not significantly different from those measured at the O-Buoys. It is notable that ~ 2/3 of the temperature averages along the trajectories were above 253 K, though we acknowledge that there is a high level of uncertainty associated with using an air mass back trajectory model for such a purpose in a data sparse region (Kahl, 1993). This analysis reveals no apparent temperature dependence for O_3 depletion within the Beaufort Sea region.

Recent reports discuss the possibility that ODEs can be initiated after blowing snow events (Frieß et al., 2011; Jones et al., 2009; Yang et al., 2008, 2010), which presumably produce the availability of new saline surfaces, whether in suspended aerosol form, or through redeposition of sea salt aerosol to the physical surface. Blowing snow

ACPD
13, 30233–30285, 2013

events occur during periods of higher wind speeds ($>8\,m\,s^{-1}$) (Frieß et al., 2011), which implies that there might be a relationship between wind speed and ODEs. Figure 12a shows that ODEs observed at the O-Buoy were characterized by low measured wind speeds (median of $3.6\,m\,s^{-1}$ and a mode of $3.5\,m\,s^{-1}$), relative to what is needed for blowing snow. However, there is also a difficulty in this analysis in that, under these circumstances, when the air is most of the time at least partly depleted, such a histogram may reflect, at least in part, the normal distribution of wind speeds found in the Arctic troposphere. Therefore, for comparison, periods when O_3 was not depleted (non-ODEs) were examined (see Supplement). As shown in Fig. S5, there was no apparent difference in the modes for these distributions relative to the depleted cases. It should be noted that the wind speeds as measured by the O-Buoy reported here could be biased low (see Sect. 2.1); thus, we compare this distribution to the distribution of wind speeds as determined by HYSPLIT below.

To some extent, all ODEs with any significant duration occur upwind, at various distances. To address the possibility that the upwind wind speeds were different from those observed by the O-Buoys, the average wind speeds for each ODE were calculated from HYSPLIT backward air mass trajectories, as described in the Supplement. Wind speeds from this analysis reveal a faster median wind speed of $5\,m\,s^{-1}$, potentially consistent with ODEs occurring at somewhat higher wind speeds, but, as stated above, it is possible the O-Buoy anemometer is biased low. The wind speeds distribution from this analysis showed no clear preference for higher wind speeds for ODEs (Fig. 12). Through examination of HYSPLIT backward air mass trajectories during non-ODE periods, we found the majority of wind speeds to be between 3 and $6\,m\,s^{-1}$, similar to that for the ODE cases (Fig. S5b), showing that the wind speeds characterizing the upwind air masses observed for ODEs are not significantly different from those for non-depleted conditions. From this analysis, we found that elevated wind speed appeared to be neither a prerequisite, nor a defining characteristic for ODEs, as also found by Helmig et al. (2012) and Solberg et al. (1996).

ACPD
13, 30233–30285, 2013

4 Conclusions

The autonomous, sea ice-tethered O-Buoy was developed in part to enable observation of ODEs at the hypothesized location of their initiation, the frozen Arctic Ocean surface. Surface measurements of ambient O_3, BrO, temperature, and wind speed from five separate O-Buoy deployments were utilized to gain insights into the characteristics of ODEs observed over the Arctic Ocean.

The apparent timescales of O_3 depletion during ODEs, based on both chemistry and transport, were calculated to be shorter (median of 11 h) than previous modeled chemical estimates (e.g., Hausmann and Platt, 1994) by a factor of two or more. This observation suggests the O_3 depletion timescales are dominated by either atmospheric transport, accelerated chemical mechanisms involving higher radical levels, or novel chemical mechanisms. Spatially, the majority of the Arctic Ocean marine boundary layer is likely at least partially depleted in O_3 during spring, suggesting that O_3-depleted air masses remain intact for long periods of time after the halogen chemistry has subsided. Regions of MODEs ($O_3 < 10\,\mathrm{nmol\,mol^{-1}}$) were, on average, smaller, with a median of 282 km, compared to a median of ~ 908 km for ODEs ($O_3 \leq 15\,\mathrm{nmol\,mol^{-1}}$). An expanded network of O_3 monitors across the Arctic Ocean is required to effectively capture the spatial extent of the small, actively O_3-depleting air masses, as well as that of the larger, depleted air masses. Monte Carlo simulations supported the notion that these spatial ODE sizes are consistent with depletion upwind of the O-Buoy, followed by air mass transport to the buoy. However, the degree to which process dominates (advection vs. chemistry) is unknown, as O-Buoy observations of BrO indicate that there is some degree of chemistry involved. Thus, to further address the question of the O_3 depletion timescales, more long-term O_3 and halogen measurements over the Arctic Ocean sea ice are necessary, particularly in locations such as the East Siberian and Chukchi Seas.

There was no apparent temperature dependence observed for the presence of an ODE, and low temperatures (i.e. less than 253 K) were not required for the observation

ACPD
13, 30233–30285, 2013

of an ODE. The distribution of wind speeds local to the O-Buoy was moderately low during ODEs (mode of $\sim 3.5\,m\,s^{-1}$), showing that ODEs were primarily observed under relatively calm conditions. While higher average wind speeds (median $\sim 5\,m\,s^{-1}$) were estimated for the course of the backward air mass trajectory, we did not observe a clear preference for ODEs occurring during higher wind speeds. Concurrent measurements of blowing snow, sea salt aerosol, ozone, and halogens, in addition to wind speed, are required to better understand the relationship between wind speed and ODEs.

Supplementary material related to this article is available online at http://www.atmos-chem-phys-discuss.net/13/30233/2013/acpd-13-30233-2013-supplement.pdf.

Acknowledgements. The authors thank the NSF for the funding of both the development and deployments of the O-Buoys (grants ARC-0612331, ARC-0611992, ARC-0612047, and ARC-0612457 to P. A. Matrai, D. K. Perovich, P. B. Shepson, and W. R. Simpson, respectively), as well as for the NSF Postdoctoral Fellowship for Polar Regions Research for K. A. Pratt. Additionally, we are thankful for additional funding for O-Buoys provided by the Government of Canada Program for the International Polar Year, as part of OASIS-CANADA (Project No. MD065). We would like to also thank U. Frieß and J. Zielke at the University of Heidelberg for assistance with the inversion of the MAX-DOAS. The authors thank the NOAA Air Resources Laboratory (ARL) for the provision of the HYSPLIT transport and dispersion model used in this publication, as well as the National Sea Ice Data Center for providing access to monthly sea ice extent data. The authors are grateful to the O-Buoy* team, without whom this project would not have been possible. *The current O-Buoy team includes M. Carlsen, F. Chavez, M. Everly, G. Friederich, P. Joyce, R. Oglesbee, C. Rauschenberg, A. Sheppard, R. Stehle, B. Tupper, T. Valentic, C. Wahl, C. Williams, P. Wyss, and J. Zimmerman.

ACPD
13, 30233–30285, 2013

References

Abbatt, J. P. D., Thomas, J. L., Abrahamsson, K., Boxe, C., Granfors, A., Jones, A. E., King, M. D., Saiz-Lopez, A., Shepson, P. B., Sodeau, J., Toohey, D. W., Toubin, C., von Glasow, R., Wren, S. N., and Yang, X.: Halogen activation via interactions with environmental ice and snow in the polar lower troposphere and other regions, Atmos. Chem. Phys., 12, 6237–6271, doi:10.5194/acp-12-6237-2012, 2012.

Adams, J. W., Holmes, N. S., and Crowley, J. N.: Uptake and reaction of HOBr on frozen and dry NaCl/NaBr surfaces between 253 and 233 K, Atmos. Chem. Phys., 2, 79–91, doi:10.5194/acp-2-79-2002, 2002.

Aguzzi, A. and Rossi, M. J.: Heterogeneous hydrolysis and reaction of $BrONO_2$ and Br_2O on pure ice and ice doped with HBr, J. Phys. Chem. A, 106, 5891–5901, doi:10.1021/Jp014383e, 2002.

Albert, M. R., Grannas, A. M., Bottenheim, J., Shepson, P. B., and Perron, F. E.: Processes and properties of snow–air transfer in the high Arctic with application to interstitial ozone at Alert, Canada, Atmos. Environ., 36, 2779–2787, doi:10.1016/s1352-2310(02)00118-8, 2002.

Anlauf, K. G., Mickle, R. E., and Trivett, N. B. A.: Measurement of ozone during Polar Sunrise Experiment 1992, J. Geophys. Res., 99, 25345–25353, doi:10.1029/94jd01312, 1994.

Barrie, L. A., Bottenheim, J. W., Schnell, R. C., Crutzen, P. J., and Rasmussen, R. A.: Ozone destruction and photochemical-reactions at polar sunrise in the lower Arctic atmosphere, Nature, 334, 138–141, 1988.

Barrie, L. A., Staebler, R., Toom, D., Georgi, B., Denhartog, G., Landsberger, S., and Wu, D.: Arctic aerosol size-segregated chemical observations in relation to ozone depletion during Polar Sunrise Experiment 1992, J. Geophys. Res., 99, 25439–25451, doi:10.1029/94jd01514, 1994.

Bottenheim, J. W. and Chan, E.: A trajectory study into the origin of spring time Arctic boundary layer ozone depletion, J. Geophys. Res., 111, D19301, doi:10.1029/2006jd007055, 2006.

Bottenheim, J. W., Gallant, A. G., and Brice, K. A.: Measurements of NO_y species and O_3 at 82° N latitude, Geophys. Res. Lett., 13, 113–116, doi:10.1029/GL013i002p00113, 1986.

Bottenheim, J. W., Fuentes, J. D., Tarasick, D. W., and Anlauf, K. G.: Ozone in the Arctic lower troposphere during winter and spring 2000 (ALERT2000), Atmos. Environ., 36, 2535–2544, doi:10.1016/s1352-2310(02)00121-8, 2002.

ACPD
13, 30233–30285, 2013

Bottenheim, J. W., Netcheva, S., Morin, S., and Nghiem, S. V.: Ozone in the boundary layer air over the Arctic Ocean: measurements during the TARA transpolar drift 2006–2008, Atmos. Chem. Phys., 9, 4545–4557, doi:10.5194/acp-9-4545-2009, 2009.

Boudries, H. and Bottenheim, J. W.: Cl and Br atom concentrations during a surface boundary layer ozone depletion event in the Canadian high Arctic, Geophys. Res. Lett., 27, 517–520, doi:10.1029/1999gl011025, 2000.

Calvert, J. G. and Lindberg, S. E.: Potential influence of iodine-containing compounds on the chemistry of the troposphere in the polar spring. I. Ozone depletion, Atmos. Environ., 38, 5087–5104, doi:10.1016/j.atmosenv.2004.05.049, 2004.

Carlson, D., Donohoue, D., Platt, U., and Simpson, W. R.: A low power automated MAX-DOAS instrument for the Arctic and other remote unmanned locations, Atmos. Meas. Tech., 3, 429–439, doi:10.5194/amt-3-429-2010, 2010.

Cho, H., Shepson, P. B., Barrie, L. A., Cowin, J. P., and Zaveri, R.: NMR investigation of the quasi-brine layer in ice/brine mixtures, J. Phys. Chem. B, 106, 11226–11232, doi:10.1021/Jp020449+, 2002.

Choi, S., Wang, Y., Salawitch, R. J., Canty, T., Joiner, J., Zeng, T., Kurosu, T. P., Chance, K., Richter, A., Huey, L. G., Liao, J., Neuman, J. A., Nowak, J. B., Dibb, J. E., Weinheimer, A. J., Diskin, G., Ryerson, T. B., da Silva, A., Curry, J., Kinnison, D., Tilmes, S., and Levelt, P. F.: Analysis of satellite-derived Arctic tropospheric BrO columns in conjunction with aircraft measurements during ARCTAS and ARCPAC, Atmos. Chem. Phys., 12, 1255–1285, doi:10.5194/acp-12-1255-2012, 2012.

Deutschmann, T., Beirle, S., Frieß, U., Grzegorski, M., Kern, C., Kritten, L., Platt, U., Prados-Román, C., Pukite, J., Wagner, T., Werner, B., and Pfeilsticker, K.: The Monte Carlo atmospheric radiative transfer model McArtim: Introduction and validation of Jacobians and 3-D features, J. Quant. Spectrosc. Ra., 112, 1119–1137, 2011.

Draxler, R. R.: HYSPLIT 4 users's guide, US Dept. of Commerce, National Oceanic and Atmospheric Administration, Environmental Research Laboratories, Air Resources Laboratory, Silver Spring, MD, 1999.

Draxler, R. R. and Hess, G. D.: Description of the HYSPLIT 4 modeling system. NOAA Tech. Memo. ERL ARL-224, NOAA Air Resources Laboratory, Silver Spring, MD, 1997.

Draxler, R. R. and Hess, G. D.: An overview of the HYSPLIT 4 modeling system of trajectories, dispersion, and deposition, Aust. Meteor. Mag., 47, 295–308, 1998.

ACPD
13, 30233–30285, 2013

Fan, S. M. and Jacob, D. J.: Surface ozone depletion in Arctic spring sustained by bromine reactions on aerosols, Nature, 359, 522–524, doi:10.1038/359522a0, 1992.

Foster, K. L., Plastridge, R. A., Bottenheim, J. W., Shepson, P. B., Finlayson-Pitts, B. J., and Spicer, C. W.: The role of Br_2 and BrCl in surface ozone destruction at polar sunrise, Science, 291, 471–474, doi:10.1126/science.291.5503.471, 2001.

Frieß, U., Monks, P. S., Remedios, J. J., Rozanov, A., Sinreich, R., Wagner, T., and Platt, U.: MAX-DOAS O_4 measurements: a new technique to derive information on atmospheric aerosols: 2. Modeling studies, J. Geophys. Res., 111, D14203, doi:10.1029/2005JD006618, 2006.

Frieß, U., Sihler, H., Sander, R., Pöhler, D., Yilmaz, S., and Platt, U.: The vertical distribution of BrO and aerosols in the Arctic: measurements by active and passive differential optical absorption spectroscopy, J. Geophys. Res., 116, D00R04, doi:10.1029/2011jd015938, 2011.

Gauss, M., Myhre, G., Isaksen, I. S. A., Grewe, V., Pitari, G., Wild, O., Collins, W. J., Dentener, F. J., Ellingsen, K., Gohar, L. K., Hauglustaine, D. A., Iachetti, D., Lamarque, F., Mancini, E., Mickley, L. J., Prather, M. J., Pyle, J. A., Sanderson, M. G., Shine, K. P., Stevenson, D. S., Sudo, K., Szopa, S., and Zeng, G.: Radiative forcing since preindustrial times due to ozone change in the troposphere and the lower stratosphere, Atmos. Chem. Phys., 6, 575–599, doi:10.5194/acp-6-575-2006, 2006.

Gilman, J. B., Burkhart, J. F., Lerner, B. M., Williams, E. J., Kuster, W. C., Goldan, P. D., Murphy, P. C., Warneke, C., Fowler, C., Montzka, S. A., Miller, B. R., Miller, L., Oltmans, S. J., Ryerson, T. B., Cooper, O. R., Stohl, A., and de Gouw, J. A.: Ozone variability and halogen oxidation within the Arctic and sub-Arctic springtime boundary layer, Atmos. Chem. Phys., 10, 10223–10236, doi:10.5194/acp-10-10223-2010, 2010.

Hanson, D. R. and Ravishankara, A. R.: Heterogeneous chemistry of bromine species in sulfuric-acid under stratospheric conditions, Geophys. Res. Lett., 22, 385–388, doi:10.1029/94gl03379, 1995.

Hausmann, M. and Platt, U.: Spectroscopic measurement of bromine oxide and ozone in the high Arctic during Polar Sunrise Experiment 1992, J. Geophys. Res., 99, 25399–25413, doi:10.1029/94jd01314, 1994.

Helmig, D., Cohen, L. D., Bocquet, F., Oltmans, S., Grachev, A., and Neff, W.: Spring and summertime diurnal surface ozone fluxes over the polar snow at Summit, Greenland, Geophys. Res. Lett., 36, L08809, doi:10.1029/2008gl036549, 2009.

ACPD
13, 30233–30285, 2013

Helmig, D., Boylan, P., Johnson, B., Oltmans, S., Fairall, C., Staebler, R., Weinheimer, A., Orlando, J., Knapp, D. J., Montzka, D. D., Flocke, F., Frieß, U., Sihler, H., and Shepson, P. B.: Ozone dynamics and snow-atmosphere exchanges during ozone depletion events at Barrow, Alaska, J. Geophys. Res., 117, D20303, doi:10.1029/2012jd017531, 2012.

Hönninger, G., Leser, H., Sebastián, O., and Platt, U.: Ground-based measurements of halogen oxides at the Hudson Bay by active longpath DOAS and passive MAX-DOAS, Geophys. Res. Lett., 31, L04111, doi:10.1029/2003gl018982, 2004a.

Hönninger, G., von Friedeburg, C., and Platt, U.: Multi axis differential optical absorption spectroscopy (MAX-DOAS), Atmos. Chem. Phys., 4, 231–254, doi:10.5194/acp-4-231-2004, 2004b.

Hopper, J. F., Peters, B., Yokouchi, Y., Niki, H., Jobson, B. T., Shepson, P. B., and Muthuramu, K.: Chemical and meteorological observations at ice camp Swan during Polar Sunrise Experiment 1992, J. Geophys. Res., 99, 25489–25498, doi:10.1029/94JD02303, 1994.

Hopper, J. F., Barrie, L. A., Silis, A., Hart, W., Gallant, A. J., and Dryfhout, H.: Ozone and meteorology during the 1994 Polar Sunrise Experiment, J. Geophys. Res., 103, 1481–1492, 1998.

Huff, A. K. and Abbatt, J. P. D.: Kinetics and product yields in the heterogeneous reactions of HOBr with ice surfaces containing NaBr and NaCl, J. Phys. Chem. A, 106, 5279–5287, doi:10.1021/Jp014296m, 2002.

Hutterli, M. A., McConnell, J. R., Stewart, R. W., Jacobi, H. W., and Bales, R. C.: Impact of temperature-driven cycling of hydrogen peroxide (H_2O_2) between air and snow on the planetary boundary layer, J. Geophys. Res., 106, 15395–15404, doi:10.1029/2001jd900102, 2001.

Jacobi, H. W., Frey, M. M., Hutterli, M. A., Bales, R. C., Schrems, O., Cullen, N. J., Steffen, K., and Koehler, C.: Measurements of hydrogen peroxide and formaldehyde exchange between the atmosphere and surface snow at Summit, Greenland, Atmos. Environ., 36, 2619–2628, doi:10.1016/S1352-2310(02)00106-1, 2002.

Jacobi, H. W., Kaleschke, L., Richter, A., Rozanov, A., and Burrows, J. P.: Observation of a fast ozone loss in the marginal ice zone of the Arctic Ocean, J. Geophys. Res., 111, D15309, doi:10.1029/2005jd006715, 2006.

Jacobi, H. W., Morin, S., and Bottenheim, J. W.: Observation of widespread depletion of ozone in the springtime boundary layer of the central Arctic linked to mesoscale synoptic conditions, J. Geophys. Res., 115, D17302, doi:10.1029/2010jd013940, 2010.

ACPD
13, 30233–30285, 2013

Jaeschke, W., Salkowski, T., Dierssen, J. P., Trumbach, J. V., Krischke, U., and Günther, A.: Measurements of trace substances in the Arctic troposphere as potential precursors and constituents of Arctic haze, J. Atmos. Chem., 34, 291–319, 1999.

Jobson, B. T., Niki, H., Yokouchi, Y., Bottenheim, J., Hopper, F., and Leaitch, R.: Measurements of C_2-C_6 hydrocarbons during the Polar Sunrise 1992 Experiment – evidence for Cl atom and Br atom chemistry, J. Geophys. Res., 99, 25355–25368, doi:10.1029/94JD01243, 1994.

Jones, A. E., Anderson, P. S., Begoin, M., Brough, N., Hutterli, M. A., Marshall, G. J., Richter, A., Roscoe, H. K., and Wolff, E. W.: BrO, blizzards, and drivers of polar tropospheric ozone depletion events, Atmos. Chem. Phys., 9, 4639–4652, doi:10.5194/acp-9-4639-2009, 2009.

Jones, A. E., Wolff, E. W., Brough, N., Bauguitte, S. J.-B., Weller, R., Yela, M., Navarro-Comas, M., Ochoa, H. A., and Theys, N.: The spatial scale of ozone depletion events derived from an autonomous surface ozone network in coastal Antarctica, Atmos. Chem. Phys., 13, 1457–1467, doi:10.5194/acp-13-1457-2013, 2013.

Kahl, J. D.: A cautionary note on the use of air trajectories in interpreting atmospheric chemistry measurements, Atmos. Environ. A, 27, 3037–3038, 1993.

Knepp, T. N., Bottenheim, J., Carlsen, M., Carlson, D., Donohoue, D., Friederich, G., Matrai, P. A., Netcheva, S., Perovich, D. K., Santini, R., Shepson, P. B., Simpson, W., Valentic, T., Williams, C., and Wyss, P. J.: Development of an autonomous sea ice tethered buoy for the study of ocean-atmosphere-sea ice-snow pack interactions: the O-buoy, Atmos. Meas. Tech., 3, 249–261, doi:10.5194/amt-3-249-2010, 2010.

Koo, J.-H., Wang, Y., Kurosu, T. P., Chance, K., Rozanov, A., Richter, A., Oltmans, S. J., Thompson, A. M., Hair, J. W., Fenn, M. A., Weinheimer, A. J., Ryerson, T. B., Solberg, S., Huey, L. G., Liao, J., Dibb, J. E., Neuman, J. A., Nowak, J. B., Pierce, R. B., Natarajan, M., and Al-Saadi, J.: Characteristics of tropospheric ozone depletion events in the Arctic spring: analysis of the ARCTAS, ARCPAC, and ARCIONS measurements and satellite BrO observations, Atmos. Chem. Phys., 12, 9909–9922, doi:10.5194/acp-12-9909-2012, 2012.

Kwok, R., Cunningham, G. F., Wensnahan, M., Rigor, I., Zwally, H. J., and Yi, D.: Thinning and volume loss of the Arctic Ocean sea ice cover: 2003–2008, J. Geophys. Res., 114, C07005, doi:10.1029/2009jc005312, 2009.

Le Bras, G. and Platt, U.: A possible mechanism for combined chlorine and bromine catalyzed destruction of tropospheric ozone in the arctic, Geophys. Res. Lett., 22, 599–602, doi:10.1029/94gl03334, 1995.

ACPD
13, 30233–30285, 2013

Leaitch, W. R., Barrie, L. A., Bottenheim, J. W., Li, S. M., Shepson, P. B., Muthuramu, K., and Yokouchi, Y.: Airborne observations related to ozone depletion at polar sunrise, J. Geophys. Res., 99, 25499–25517, 1994.

Lehrer, E., Hönninger, G., and Platt, U.: A one dimensional model study of the mechanism of halogen liberation and vertical transport in the polar troposphere, Atmos. Chem. Phys., 4, 2427–2440, doi:10.5194/acp-4-2427-2004, 2004.

Mahajan, A. S., Shaw, M., Oetjen, H., Hornsby, K. E., Carpenter, L. J., Kaleschke, L., Tian-Kunze, X., Lee, J. D., Moller, S. J., Edwards, P., Commane, R., Ingham, T., Heard, D. E., and Plane, J. M. C.: Evidence of reactive iodine chemistry in the Arctic boundary layer, J. Geophys. Res., 115, D20303, doi:10.1029/2009jd013665, 2010.

Martinez, M., Arnold, T., and Perner, D.: The role of bromine and chlorine chemistry for arctic ozone depletion events in Ny-Ålesund and comparison with model calculations, Ann. Geophys., 17, 941–956, doi:10.1007/s00585-999-0941-4, 1999.

Michalowski, B. A., Francisco, J. S., Li, S.-M., Barrie, L. A., Bottenheim, J. W., and Shepson, P. B.: A computer model study of multiphase chemistry in the Arctic boundary layer during polar sunrise, J. Geophys. Res., 105, 15131–15145, doi:10.1029/2000jd900004, 2000.

Miller, H. L., Weaver, A., Sanders, R. W., Arpag, K., and Solomon, S.: Measurements of arctic sunrise surface ozone depletion events at Kangerlussuaq, Greenland (67° N, 51° W), Tellus B, 49, 496–509, doi:10.1034/j.1600-0889.49.issue5.6.x, 1997.

Morin, S., Hönninger, G. H., Staebler, R. M., and Bottenheim, J. W.: A high time resolution study of boundary layer ozone chemistry and dynamics over the Arctic Ocean near Alert, Nunavut, Geophys. Res. Lett., 32, L08809, doi:10.1029/2004gl022098, 2005.

Neuman, J. A., Nowak, J. B., Huey, L. G., Burkholder, J. B., Dibb, J. E., Holloway, J. S., Liao, J., Peischl, J., Roberts, J. M., Ryerson, T. B., Scheuer, E., Stark, H., Stickel, R. E., Tanner, D. J., and Weinheimer, A.: Bromine measurements in ozone depleted air over the Arctic Ocean, Atmos. Chem. Phys., 10, 6503–6514, doi:10.5194/acp-10-6503-2010, 2010.

Nghiem, S. V., Rigor, I. G., Richter, A., Burrows, J. P., Shepson, P. B., Bottenheim, J., Barber, D. G., Steffen, A., Latonas, J., Wang, F. Y., Stern, G., Clemente-Colon, P., Martin, S., Hall, D. K., Kaleschke, L., Tackett, P., Neumann, G., and Asplin, M. G.: Field and satellite observations of the formation and distribution of Arctic atmospheric bromine above a rejuvenated sea ice cover, J. Geophys. Res., 117, D00S05, doi:10.1029/2011JD016268, 2012.

ACPD
13, 30233–30285, 2013

Oltmans, S. J., Johnson, B. J., and Harris, J. M.: Springtime boundary layer ozone depletion at Barrow, Alaska: meteorological influence, year-to-year variation, and long-term change, J. Geophys. Res., 117, D00R18, doi:10.1029/2011jd016889, 2012.

Piot, M. and von Glasow, R.: The potential importance of frost flowers, recycling on snow, and open leads for ozone depletion events, Atmos. Chem. Phys., 8, 2437–2467, doi:10.5194/acp-8-2437-2008, 2008.

Piot, M. and von Glasow, R.: Modelling the multiphase near-surface chemistry related to ozone depletions in polar spring, J. Atmos. Chem., 64, 77–105, doi:10.1007/s10874-010-9170-1, 2009.

Pöhler, D., Vogel, L., Frieß, U., and Platt, U.: Observation of halogen species in the Amundsen Gulf, Arctic, by active long-path differential optical absorption spectroscopy, P. Natl. Acad. Sci. USA, 107, 6582–6587, doi:10.1073/pnas.0912231107, 2010.

Pratt, K. A., Custard, K. D., Shepson, P. B., Douglas, T. A., Pöhler, D., General, S., Zielcke, J., Simpson, W. R., Platt, U., Tanner, D. J., Huey, G. L., Carlsen, M., and Stirm, B. H.: Photochemical production of molecular bromine in Arctic surface snowpacks, Nat. Geosci., 6, 351–356, doi:10.1038/ngeo1779, 2013.

Richter, A., Wittrock, F., Eisinger, M., and Burrows, J. P.: GOME observations of tropospheric BrO in northern hemispheric spring and summer 1997, Geophys. Res. Lett., 25, 2683–2686, 1998.

Ridley, B. A., Atlas, E. L., Montzka, D. D., Browell, E. V., Cantrell, C. A., Blake, D. R., Blake, N. J., Cinquini, L., Coffey, M. T., Emmons, L. K., Cohen, R. C., DeYoung, R. J., Dibb, J. E., Eisele, F. L., Flocke, F. M., Fried, A., Grahek, F. E., Grant, W. B., Hair, J. W., Hannigan, J. W., Heikes, B. J., Lefer, B. L., Mauldin, R. L., Moody, J. L., Shetter, R. E., Snow, J. A., Talbot, R. W., Thornton, J. A., Walega, J. G., Weinheimer, A. J., Wert, B. P., and Wimmers, A. J.: Ozone depletion events observed in the high latitude surface layer during the TOPSE aircraft program, J. Geophys. Res., 108, 8356, doi:10.1029/2001jd001507, 2003.

Rodgers, C. D.: Inverse Methods for Atmospheric Sounding: Theory and Practice, Series on Atmospheric, Oceanic, and Planetary Physics, edited by: Taylor, F. W., World Scientific Publishing, 2000.

Saiz-Lopez, A., Mahajan, A. S., Salmon, R. A., Bauguitte, S. J. B., Jones, A. E., Roscoe, H. K., and Plane, J. M. C.: Boundary layer halogens in coastal Antarctica, Science, 317, 348–351, doi:10.1126/Science.1141408, 2007.

ACPD
13, 30233–30285, 2013

Salawitch, R. J., Canty, T., Kurosu, T., Chance, K., Liang, Q., da Silva, A., Pawson, S., Nielsen, J. E., Rodriguez, J. M., Bhartia, P. K., Liu, X., Huey, L. G., Liao, J., Stickel, R. E., Tanner, D. J., Dibb, J. E., Simpson, W. R., Donohoue, D., Weinheimer, A., Flocke, F., Knapp, D., Montzka, D., Neuman, J. A., Nowak, J. B., Ryerson, T. B., Oltmans, S., Blake, D. R., Atlas, E. L., Kinnison, D. E., Tilmes, S., Pan, L. L., Hendrick, F., Van Roozendael, M., Kreher, K., Johnston, P. V., Gao, R. S., Johnson, B., Bui, T. P., Chen, G., Pierce, R. B., Crawford, J. H., and Jacob, D. J.: A new interpretation of total column BrO during Arctic spring, Geophys. Res. Lett., 37, L21805, doi:10.1029/2010GL043798, 2010.

Schall, C. and Heumann, K. G.: GC determination of volatile organoiodine and organobromine compounds in Arctic seawater and air samples, Fresenius. J. Anal. Chem., 346, 717–722, doi:10.1007/bf00321279, 1993.

Seabrook, J. A., Whiteway, J., Staebler, R. M., Bottenheim, J. W., Komguem, L., Gray, L. H., Barber, D., and Asplin, M.: LIDAR measurements of Arctic boundary layer ozone depletion events over the frozen Arctic Ocean, J. Geophys. Res., 116, D00S02, doi:10.1029/2011JD016335, 2011.

Seabrook, J. A., Whiteway, J. A., Gray, L. H., Staebler, R., and Herber, A.: Airborne lidar measurements of surface ozone depletion over Arctic sea ice, Atmos. Chem. Phys., 13, 6023–6029, doi:10.5194/acp-13-6023-2013, 2013.

Sheridan, P. J., Schnell, R. C., Zoller, W. H., Carlson, N. D., Rasmussen, R. A., Harris, J. M., and Sievering, H.: Composition of Br-containing aerosols and cases related to boundary-layer ozone destruction in the Arctic, Atmos. Environ. A, 27, 2839–2849, 1993.

Simpson, W. R., Alvarez-Aviles, L., Douglas, T. A., Sturm, M., and Dominé, F.: Halogens in the coastal snow pack near Barrow, Alaska: evidence for active bromine air-snow chemistry during springtime, Geophys. Res. Lett., 32, L04811, doi:10.1029/2004gl021748, 2005.

Simpson, W. R., Carlson, D., Hönninger, G., Douglas, T. A., Sturm, M., Perovich, D., and Platt, U.: First-year sea-ice contact predicts bromine monoxide (BrO) levels at Barrow, Alaska better than potential frost flower contact, Atmos. Chem. Phys., 7, 621–627, doi:10.5194/acp-7-621-2007, 2007a.

Simpson, W. R., von Glasow, R., Riedel, K., Anderson, P., Ariya, P., Bottenheim, J., Burrows, J., Carpenter, L. J., Frieß, U., Goodsite, M. E., Heard, D., Hutterli, M., Jacobi, H.-W., Kaleschke, L., Neff, B., Plane, J., Platt, U., Richter, A., Roscoe, H., Sander, R., Shepson, P., Sodeau, J., Steffen, A., Wagner, T., and Wolff, E.: Halogens and their role in polar boundary-

ACPD
13, 30233–30285, 2013

layer ozone depletion, Atmos. Chem. Phys., 7, 4375–4418, doi:10.5194/acp-7-4375-2007, 2007b.
Solberg, S., Schmidbauer, N., Semb, A., Stordal, F., and Hov, O.: Boundary-layer ozone depletion as seen in the Norwegian Arctic in Spring, J. Atmos. Chem., 23, 301–332, doi:10.1007/Bf00055158, 1996.
Stephens, C. R.: Studies of tropospheric halogen radical chemistry during ozone and mercury depletion events in the Arctic, Ph.D., Chemistry, Purdue University, West Lafayette, IN, 356 pp., 2012.
Stephens, C. R., Shepson, P. B., Liao, J., Huey, L. G., Apel, E. C., Cantrell, C., Flocke, F., Fried, A., Hall, S. R., Hornbrook, R. S., Knapp, D. J., Mauldin III, R. L., Montzka, D. D., Sive, B. C., Ullmann, K., Weibring, P., and Weinheimer, A.: Interactions of bromine, chlorine, and iodine photochemistry during ozone depletions in Barrow, Alaska, in preparation, 2013a.
Stephens, C. R., Shepson, P. B., Liao, J., Huey, L. G., and Cantrell, C.: Bromine atom production and chain propagation during springtime Arctic ozone depletion events in Barrow, Alaska, in preparation, 2013b.
Strong, C., Fuentes, J. D., Davis, R. E., and Bottenheim, J. W.: Thermodynamic attributes of Arctic boundary layer ozone depletion, Atmos. Environ., 36, 2641–2652, 2002.
Sumner, A. L. and Shepson, P. B.: Snowpack production of formaldehyde and its effect on the Arctic troposphere, Nature, 398, 230–233, 1999.
Sumner, A. L., Shepson, P. B., Grannas, A. M., Bottenheim, J. W., Anlauf, K. G., Worthy, D., Schroeder, W. H., Steffen, A., Dominé, F., Perrier, S., and Houdier, S.: Atmospheric chemistry of formaldehyde in the Arctic troposphere at Polar Sunrise, and the influence of the snowpack, Atmos. Environ., 36, 2553–2562, doi:10.1016/S1352-2310(02)00105-X, 2002.
Tang, T. and McConnell, J. C.: Autocatalytic release of bromine from Arctic snow pack during polar sunrise, Geophys. Res. Lett., 23, 2633–2636, doi:10.1029/96gl02572, 1996.
Tarasick, D. W. and Bottenheim, J. W.: Surface ozone depletion episodes in the Arctic and Antarctic from historical ozonesonde records, Atmos. Chem. Phys., 2, 197–205, doi:10.5194/acp-2-197-2002, 2002.
Theys, N., Van Roozendael, M., Hendrick, F., Yang, X., De Smedt, I., Richter, A., Begoin, M., Errera, Q., Johnston, P. V., Kreher, K., and De Mazière, M.: Global observations of tropospheric BrO columns using GOME-2 satellite data, Atmos. Chem. Phys., 11, 1791–1811, doi:10.5194/acp-11-1791-2011, 2011.

ACPD
13, 30233–30285, 2013

Thompson, A. M.: The oxidizing capacity of the Earths atmosphere – probable past and future changes, Science, 256, 1157–1165, 1992.
Toyota, K., McConnell, J. C., Lupu, A., Neary, L., McLinden, C. A., Richter, A., Kwok, R., Semeniuk, K., Kaminski, J. W., Gong, S.-L., Jarosz, J., Chipperfield, M. P., and Sioris, C. E.: Analysis of reactive bromine production and ozone depletion in the Arctic boundary layer using 3-D simulations with GEM-AQ: inference from synoptic-scale patterns, Atmos. Chem. Phys., 11, 3949–3979, doi:10.5194/acp-11-3949-2011, 2011.
Tuckermann, M., Ackermann, R., Gölz, C., Lorenzen-Schmidt, H., Senne, T., Stutz, J., Trost, B., Unold, W., and Platt, U.: DOAS-observation of halogen radical-catalysed arctic boundary layer ozone destruction during the ARCTOC-campaigns 1995 and 1996 in Ny-Ålesund, Spitsbergen, Tellus B, 49, 533–555, 1997.
Vogt, R., Crutzen, P. J., and Sander, R.: A mechanism for halogen release from sea-salt aerosol in the remote marine boundary layer, Nature, 383, 327–330, 1996.
Wennberg, P.: Atmospheric chemistry – bromine explosion, Nature, 397, 299–301, doi:10.1038/16805, 1999.
Yang, X., Pyle, J. A., and Cox, R. A.: Sea salt aerosol production and bromine release: Role of snow on sea ice, Geophys. Res. Lett., 35, L16815, doi:10.1029/2008gl034536, 2008.
Yang, X., Pyle, J. A., Cox, R. A., Theys, N., and Van Roozendael, M.: Snow-sourced bromine and its implications for polar tropospheric ozone, Atmos. Chem. Phys., 10, 7763–7773, doi:10.5194/acp-10-7763-2010, 2010.
Zeng, T., Wang, Y. H., Chance, K., Browell, E. V., Ridley, B. A., and Atlas, E. L.: Widespread persistent near-surface ozone depletion at northern high latitudes in spring, Geophys. Res. Lett., 30, 2298, doi:10.1029/2003GL018587, 2003.
Zhou, X. L., Beine, H. J., Honrath, R. E., Fuentes, J. D., Simpson, W., Shepson, P. B., and Bottenheim, J. W.: Snowpack photochemical production of HONO: a major source of OH in the Arctic boundary layer in springtime, Geophys. Res. Lett., 28, 4087–4090, doi:10.1029/2001gl013531, 2001.

ACPD
13, 30233–30285, 2013

Table 1. O-Buoy deployment locations and time periods of continuous measurements focused on herein.

O-Buoy Number	Latitude	Longitude	General Area	Dates of Continuous Measurements
1	71° N	156° W	Barrow, AK	2 Mar 2009–19 May 2009
1	77° N	135° W	Beaufort Sea	22 Mar 2010–14 Jul 2010
2	74° N	142° W	Beaufort Sea	11 Apr 2011–22 Jul 2011
3	60° N	90° W	Hudson Bay	22 Feb 2010–27 Mar 2010
4	78° N	112° W	Borden Island, Nunavut, Canada	4 Apr 2010–30 Apr 2010

ACPD
13, 30233–30285, 2013

Table 2. Cross sections used in spectral analysis. Each cross section is convolved using an instrument function determined by the 334 nm Hg peak.

Species	Cross Section Reference
BrO (228 K)	Wilmouth et al. (1999)
O_3 (243 K)	Malicet et al. (1995)
NO_2 (220 K)	Vandaele et al. (1998)
O_4	Hermans et al. (2001)
Ring	Determined from zenith spectra using Chance and Spurr (1997)

ACPD
13, 30233–30285, 2013

Table 3. Average BrO mole fractions during periods of O_3 decrease from O-Buoy2 MAX-DOAS, the corresponding propagated errors, and the estimated BrO required for the observed O_3 depletion timescales based on Eq. (5) (Sect. 3.1).

ODE start time (UTC)	O_3 decrease stop time (UTC)	Observed τ_{O_3} (h)	Average observed BrO (pmol mol^{-1})	Measurement uncertainty (pmol mol^{-1})	Estimated BrO required from observed τ_{O_3} (pmol mol^{-1})
15 Apr 2011 18:47	16 Apr 2011 06:41	10.5	7.2	3.5	18.6
19 Apr 2011 04:15	19 Apr 2011 04:53	0.5	5.4	3.5	121.8
26 Apr 2011 14:46	26 Apr 2011 22:29	16.2	5.2	3.2	15.7
3 May 2011 11:37	3 May 2011 14:50	1.6	2.6	2.3	35.5
6 May 2011 12:58	7 May 2011 21:32	11.8	5	3.5	16.1
26 May 2011 21:22	28 May 2011 00:59	40.6	0.9	3.2	10.3

ACPD
13, 30233–30285, 2013

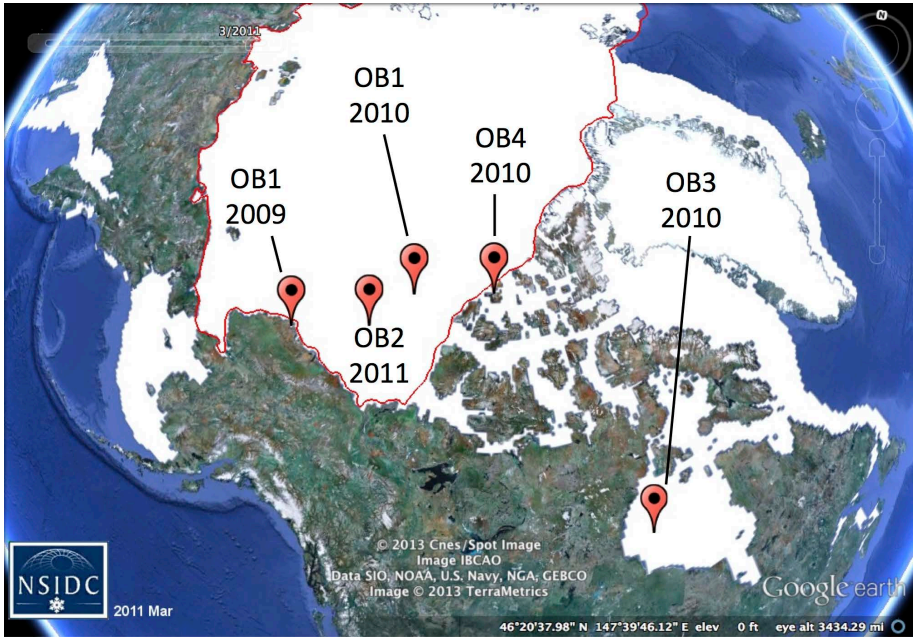

Fig. 1. Map of locations at which various O-Buoys (abbreviated OB) were deployed between 2009–2011. For the coordinates, see Table 1. Sea ice extent image is for the month of March 2011. Map courtesy of Google Earth, and sea ice image courtesy of the National Snow and Ice Data Center.

ACPD
13, 30233–30285, 2013

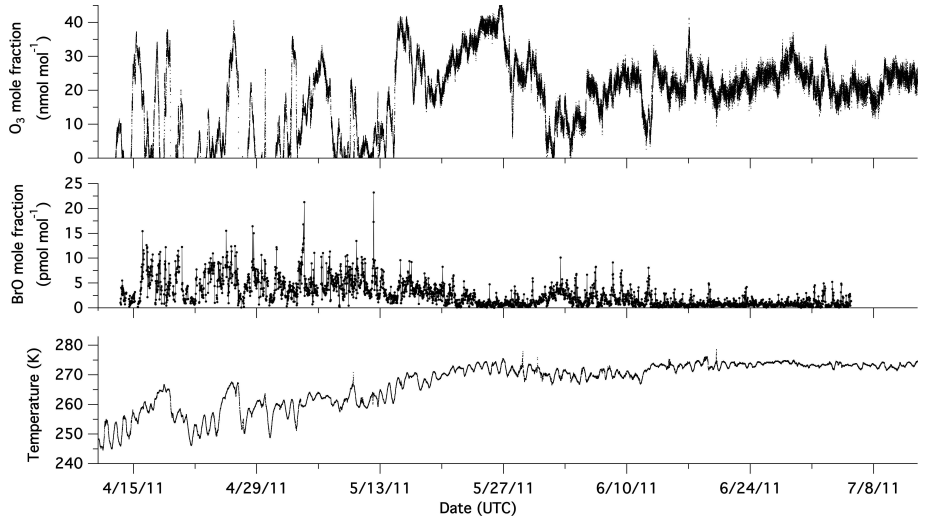

Fig. 2. Example time series of O_3, BrO, and temperature from O-Buoy2 during its deployment in the Beaufort Sea.

ACPD
13, 30233–30285, 2013

Temporal and spatial characteristics of ozone depletion events

J. W. Halfacre et al.

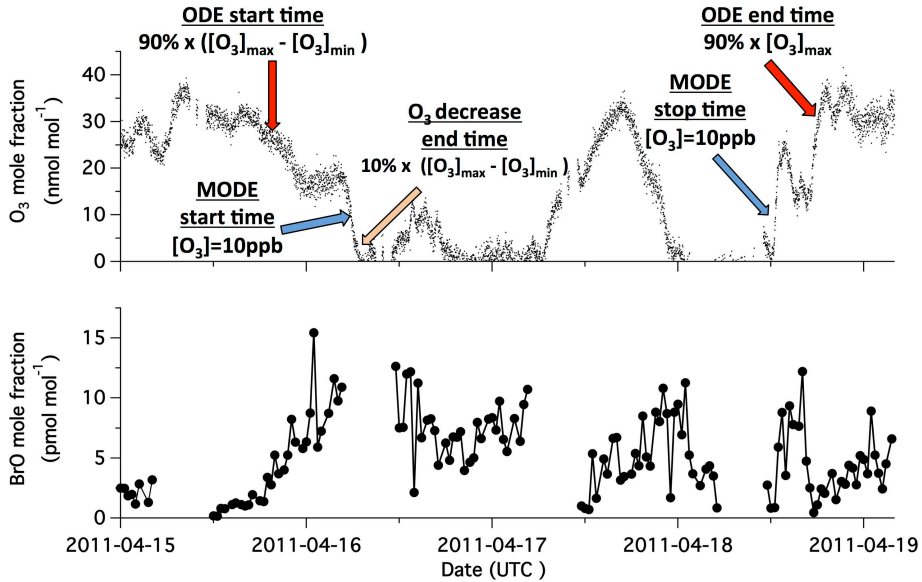

Fig. 3. Example ODE from O-Buoy2 deployment in the Beaufort Sea with ODE definitions illustrated. The brief resurgence of O_3 on 17 April does not rise above 25 nmol mol^{-1} for longer than 12 h and is thus not considered as separating two ODEs. Error bars are not displayed to more clearly show the time series. As discussed in Sect. 2.1, individual measurement errors for O_3 ranged from 2.1 to 3.5 nmol mol^{-1}, and BrO measurement errors ranged from 0.7 to 6.9 pmol mol^{-1} (median and average error ~ 3 pmol mol^{-1}).

ACPD
13, 30233–30285, 2013

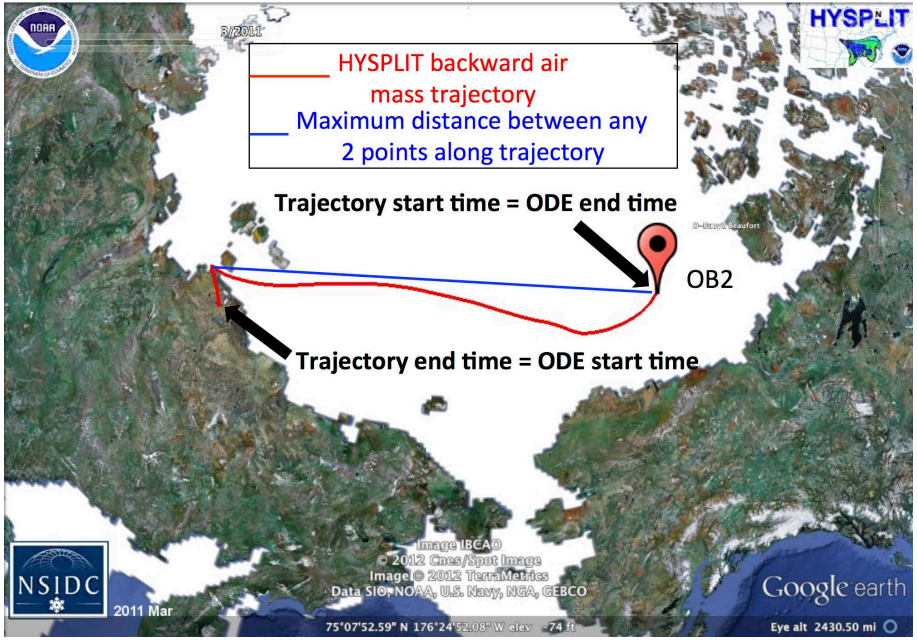

Fig. 4. Example HYSPLIT backward air mass trajectory. The HYSPLIT model was run backward starting from the ODE end time until the ODE start time. ODE spatial dimensions were determined by calculating the maximum Great Circle distance between any two points along the trajectory.

ACPD
13, 30233–30285, 2013

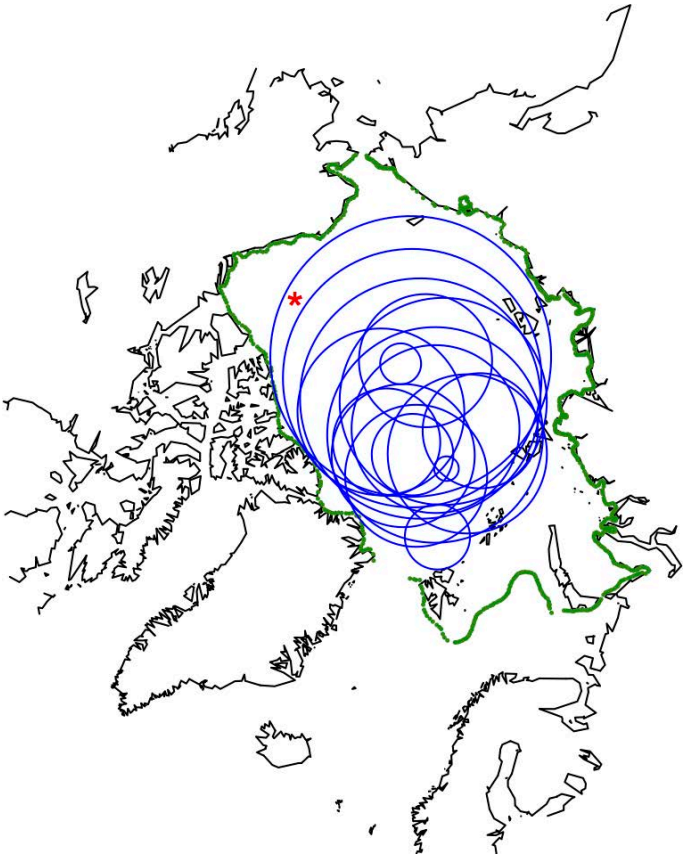

Fig. 5. Visualization of one iteration out of 2000 of the Monte Carlo experiments. The area of interest within the Arctic is defined by the green outline. Blue circles represent ODE air masses. The red star represents the average location of the O-Buoy between O-Buoys1 and 2. Seventeen different sized air masses were randomly placed simultaneously within the area of interest.

ACPD
13, 30233–30285, 2013

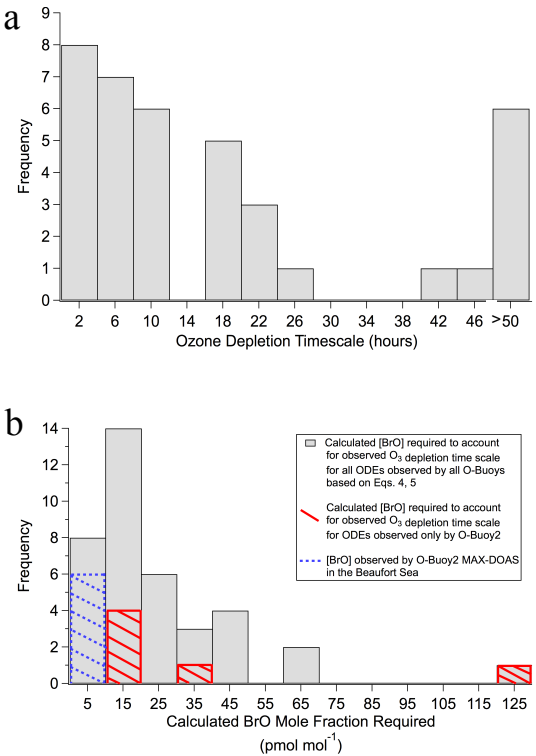

Fig. 6. (a) Histogram of the distribution of calculated O_3 depletion timescales during ODEs. To more clearly show the majority of events, the six events with τ_{O_3} greater than 50 h are grouped together on the histogram. **(b)** Calculated BrO concentrations are shown for the observed ODEs, assuming local chemistry, considering BrO and an assumed ClO mole fraction of 6 pmol mol^{-1}, and other O_3 destruction pathways, using Eq. (5) as discussed in Sect. 3.1. The mode calculated BrO mole fraction is 15 pmol mol^{-1}. Measured BrO for O-Buoy2 is shown as the blue hatched bar, and the corresponding BrO required to account for the observed ozone depletion rates for O-Buoy2 events are shown as solid red diagonal bars.

ACPD
13, 30233–30285, 2013

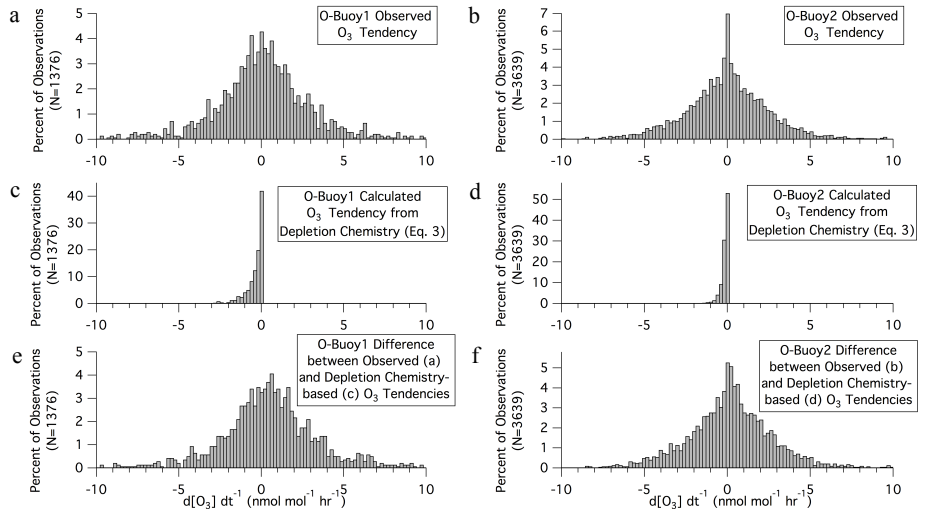

Fig. 7. Histogram of the O_3 tendency for observations from O-Buoy1 at Barrow, AK **(a, c, e)**, and O-Buoy2 in the Beaufort Sea **(b, d, f)**. Top plots (**a** and **b**) show the distributions of observed O_3 tendencies between consecutive BrO measurement points. Middle plots (**c**, **d**) represent the O_3 tendency distribution based on the depletion chemistry accounted for by Eq. (4). Bottom plots (**e**, **f**) result from the difference of the observed O_3 tendency **(a, b)** and the contributions of the chemistry accounted for by Eq. (4) **(c, d)**.

ACPD
13, 30233–30285, 2013

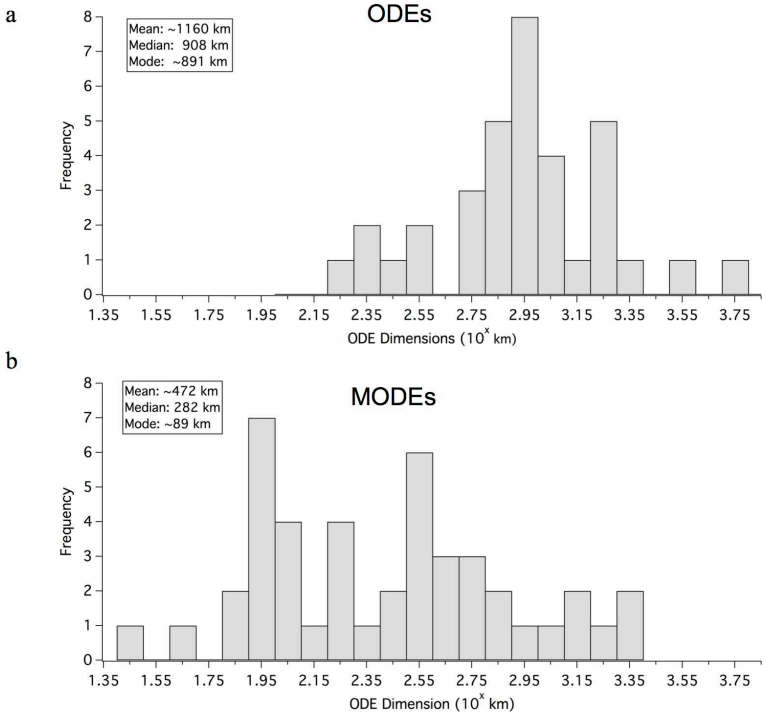

Fig. 8. (a) Histogram of ODE dimensions for all ODEs. The median of the distribution is ~ 908 km. **(b)** Histogram of dimensions of MODEs. The median of the distribution is ~ 282 km.

ACPD
13, 30233–30285, 2013

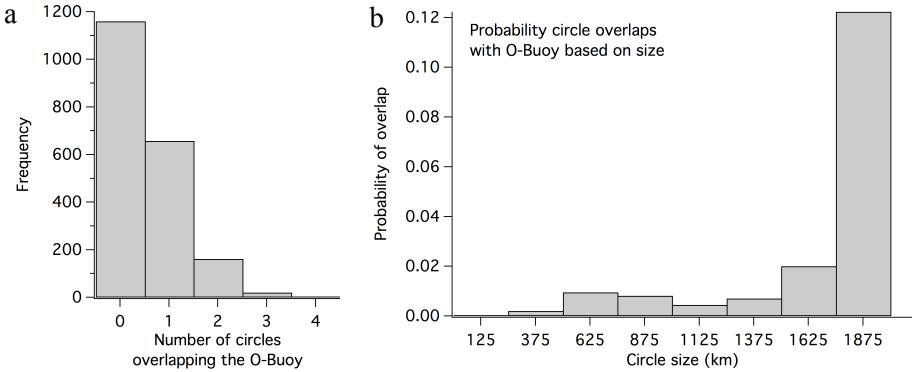

Fig. 9. Results from Monte Carlo simulation experiment. **(a)** Based on the size distribution as defined by the ODE definition ($O_3 \leq 15\,\text{pmol}\,\text{mol}^{-1}$), circular areas were shown to not overlap with the site of the O-Buoy 58 % of the time (mode = 0), followed by an overlap of one circle 33 % of the time. **(b)** Plot of the probability that an individual circle overlaps with the measurement site vs the size of the circle.

ACPD
13, 30233–30285, 2013

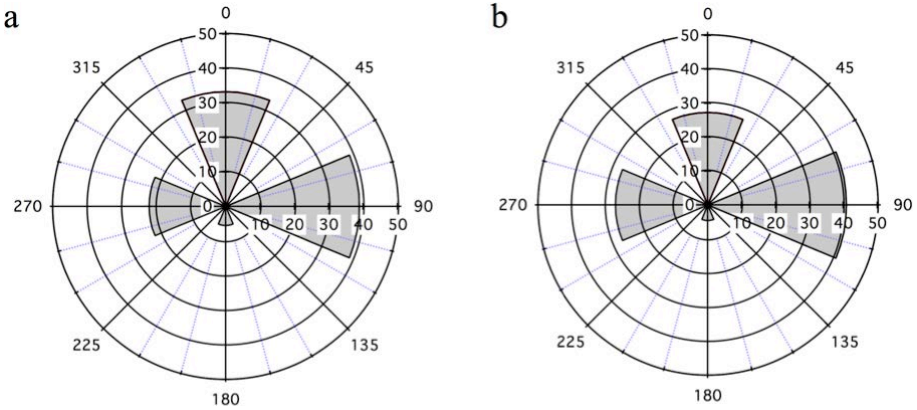

Fig. 10. Wind rose plots based on the HYSPLIT backward air mass trajectories showing measured wind direction (degrees) and frequency (%), for **(a)** ODEs and **(b)** MODEs observed during the two O-Buoy Beaufort Sea deployments (see Fig. 1).

ACPD
13, 30233–30285, 2013

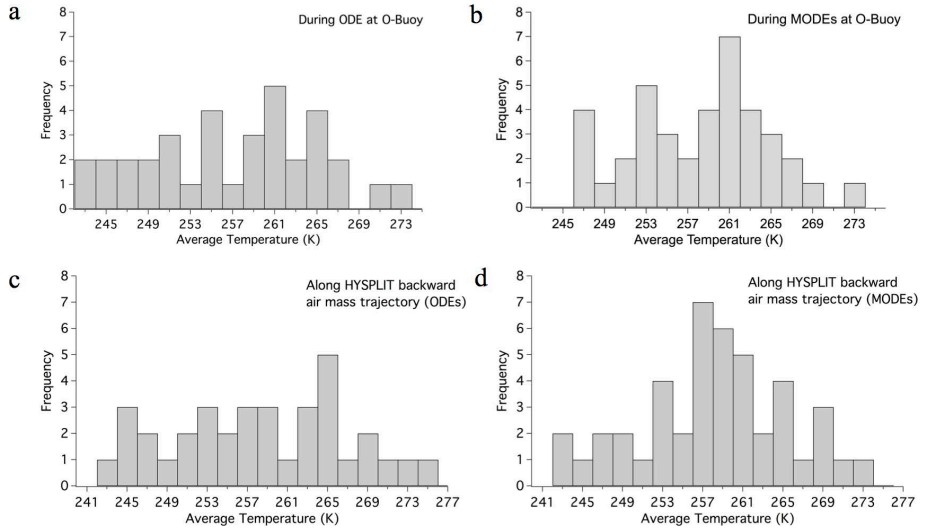

Fig. 11. (a) Histogram of the average ambient temperature measured by the O-Buoys during ODEs and **(b)** MODEs. **(c)** Histogram of the average temperature along the HYSPLIT backward air mass trajectories for ODEs and **(d)** MODEs.

ACPD
13, 30233–30285, 2013

Temporal and spatial characteristics of ozone depletion events

J. W. Halfacre et al.

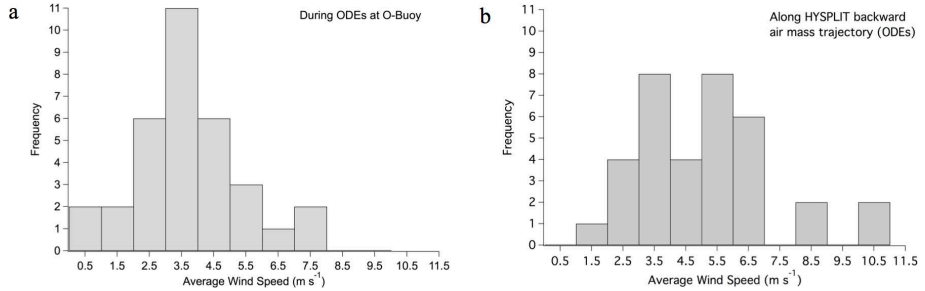

Fig. 12. (a) Histogram of the average wind speed measured by the O-Buoys during ODEs. **(b)** Histogram of average wind speeds from O_3-depleted air masses, as determined from the HYSPLIT backward air mass trajectories.

ACPD
13, 30233–30285, 2013